Lithosphere

Research Article

Removal of the Northern Paleo-Teton Range along the Yellowstone Hotspot Track

Ryan Thigpen [ID],[1] Summer J. Brown [ID],[1] Autumn L. Helfrich [ID],[1] Rachel Hoar [ID],[1] Michael McGlue [ID],[1] Edward Woolery [ID],[1] William R. Guenthner [ID],[2] Meredith L. Swallom [ID],[1] Spencer Dixon [ID],[1] and Sean Gallen [ID][3]

[1]*Department of Earth and Environmental Sciences, University of Kentucky, Lexington, KY 40506, USA*
[2]*Department of Geology, University of Illinois Urbana-Champaign, Urbana, IL 61801, USA*
[3]*Department of Geosciences, Colorado State University, Fort Collins, CO 80523, USA*

Correspondence should be addressed to Ryan Thigpen; ryan.thigpen@uky.edu

Classically held mechanisms for removing mountain topography (e.g., erosion and gravitational collapse) require 10-100 Myr or more to completely remove tectonically generated relief. Here, we propose that mountain ranges can be completely and rapidly (<2 Myr) removed by a migrating hotspot. In western North America, multiple mountain ranges, including the Teton Range, terminate at the boundary with the relatively low relief track of the Yellowstone hotspot. This abrupt transition leads to a previously untested hypothesis that preexisting mountainous topography along the track has been erased. We integrate thermochronologic data collected from the footwall of the Teton fault with flexural-kinematic modeling and length-displacement scaling to show that the paleo-Teton fault and associated Teton Range was much longer (min. original length 190-210 km) than the present topographic expression of the range front (~65 km) and extended across the modern-day Yellowstone hotspot track. These analyses also indicate that the majority of fault displacement (min. 11.4-12.6 km) and the associated footwall mountain range growth had accumulated prior to Yellowstone encroachment at ~2 Ma, leading us to interpret that eastward migration of the Yellowstone hotspot relative to stable North America led to removal of the paleo-Teton mountain topography via posteruptive collapse of the range following multiple supercaldera (VEI 8) eruptions from 2.0 Ma to 600 ka and/or an isostatic collapse response, similar to ranges north of the Snake River plain. While this extremely rapid removal of mountain ranges and adjoining basins is probably relatively infrequent in the geologic record, it has important implications for continental physiography and topography over very short time spans.

1. Introduction

Studies of mountain ranges commonly invoke erosion and extensional collapse to explain the reduction of topographic relief [1–5] and rarely do such studies consider less common, but geologically significant mechanisms such as supercalderas. In regions that have experienced a prolonged history of explosive volcanism and particularly regions impacted by supercalderas eruptions, it is useful to consider whether or not these cataclysmic mechanisms could denude or even completely diminish mountain topography where it intersects the caldera boundaries. In the Basin and Range province in the western US, the ranges generally represent the uplifted footwalls of crustal-scale normal faults [6]. In the northern Basin and Range of Idaho and Wyoming, the NNW striking crustal-scale normal faults and their associated uplifted footwall mountain blocks and adjoining half-grabens terminate where they intersect the anomalous low relief of the Snake River Plain (SRP; Figure 1). The SRP marks the ENE migration of the Yellowstone hotspot (YHS), and the truncation of Basin and Range structures on either side of the SRP leads to the hypothesis that the YHS may have somehow removed the associated mountain topography [7–10]. The Teton, Gallatin, Madison, and Centennial ranges all abut and appear to be truncated by the 2.0-0.6 Ma Yellowstone caldera and two studies [9, 10]
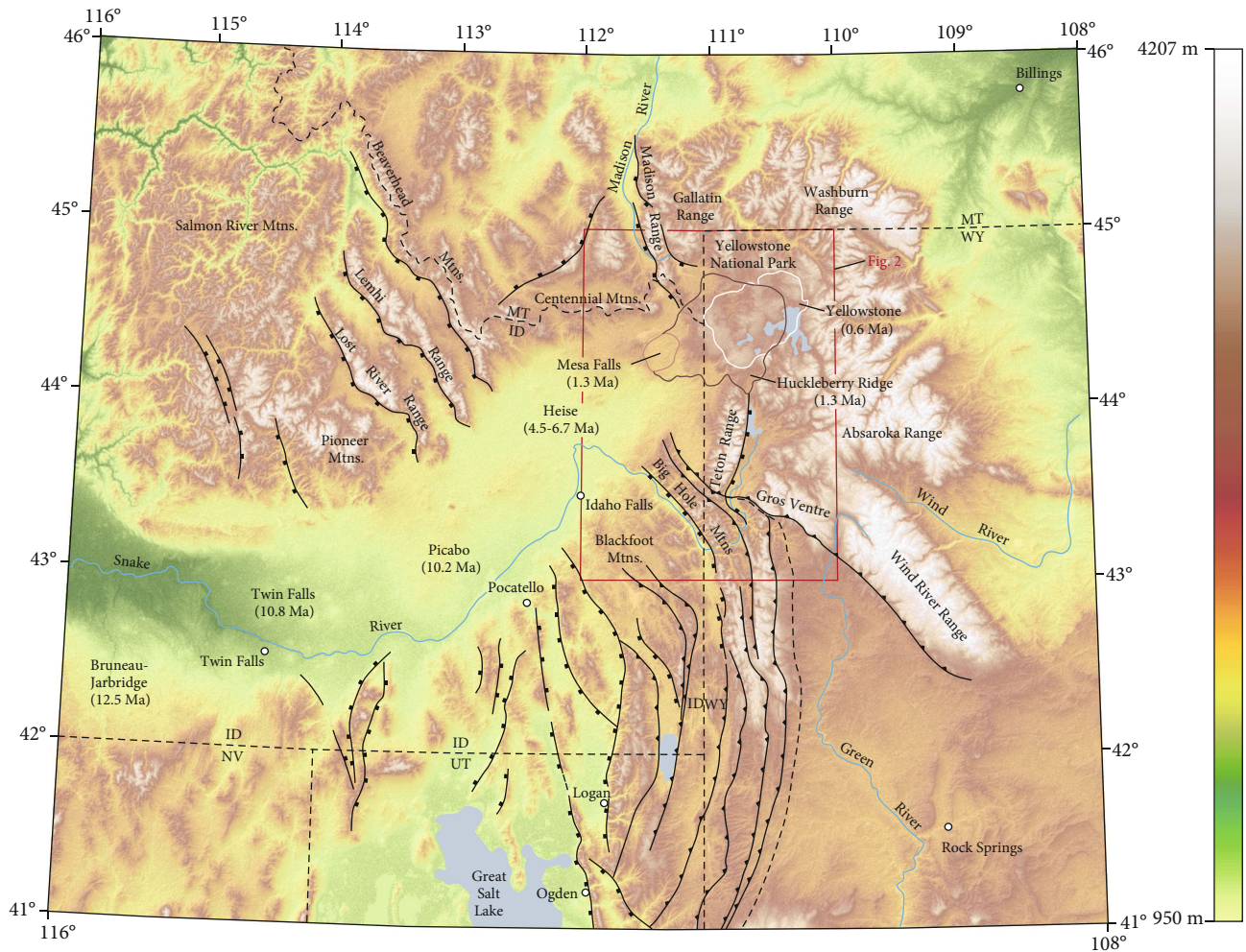
FIGURE 1: Regional digital elevation model (DEM) of the Snake River Plain in the northern Basin and Range showing the track of the Yellowstone hotspot. Positions and time intervals of the Yellowstone plume derived from [64, 65]. The Snake River Plain is the only relatively flat zone transecting the greater Rocky Mountain-Sierra Madre chain that extends from central Mexico in the south to the Canadian Yukon in the north, which we interpret to indicate a causal link between the hotspot track and the removal of topography. The position of Figure 2 is also shown.

previously speculated that the Teton and Gallatin ranges may have been initially continuous across the caldera based on their similar topographic grains and footwall strata. However, this hypothesis has remained untested and, if supported, the potential implications for fault growth, regional landscape evolution, and topographically controlled continental drainage remain unclear but could be significant.

Although it is expected that the faults and the footwall mountain ranges transected by the hotspot track would be removed and thus cannot be directly observed, it is possible to determine if there is missing fault length based on determination of maximum displacement for each fault, as there is a robust empirical relationship between the length of faults and the maximum accumulated displacement (e.g., [11] and references therein). In this scenario, if the maximum displacement accumulated on a fault can be independently determined, the displacement can be compared with empirically determined length-displacement scaling relationships to identify any potential missing fault length that may have

existed prior to migration of the hotspot along the track. Although such an exercise could be carried out for any of the ranges abutting the hotspot track, the Teton normal fault is an ideal candidate for such a test, due to the age control and delineated caldera extents of the three supercaldera events that may have affected Teton Range paleotopography. However, estimates of displacement magnitude on the Teton fault and, to a lesser extent, the long-term fault slip history, have remained varied and elusive. Additionally, the position of the Teton fault at the confluence of four tectonically unique provinces, including the Basin and Range extensional province, the Yellowstone caldera and associated Snake River Plain, the Sevier fold-and-thrust-belt, and the Laramide Gros-Ventre-Wind River uplift, has further complicated a genetic understanding of Teton fault motion.

Previous displacement estimates across the Teton fault range from 2 to 11 km ([12] and references therein). This large degree of uncertainty reflects the lack of subsurface control, the challenges of imaging through hanging wall
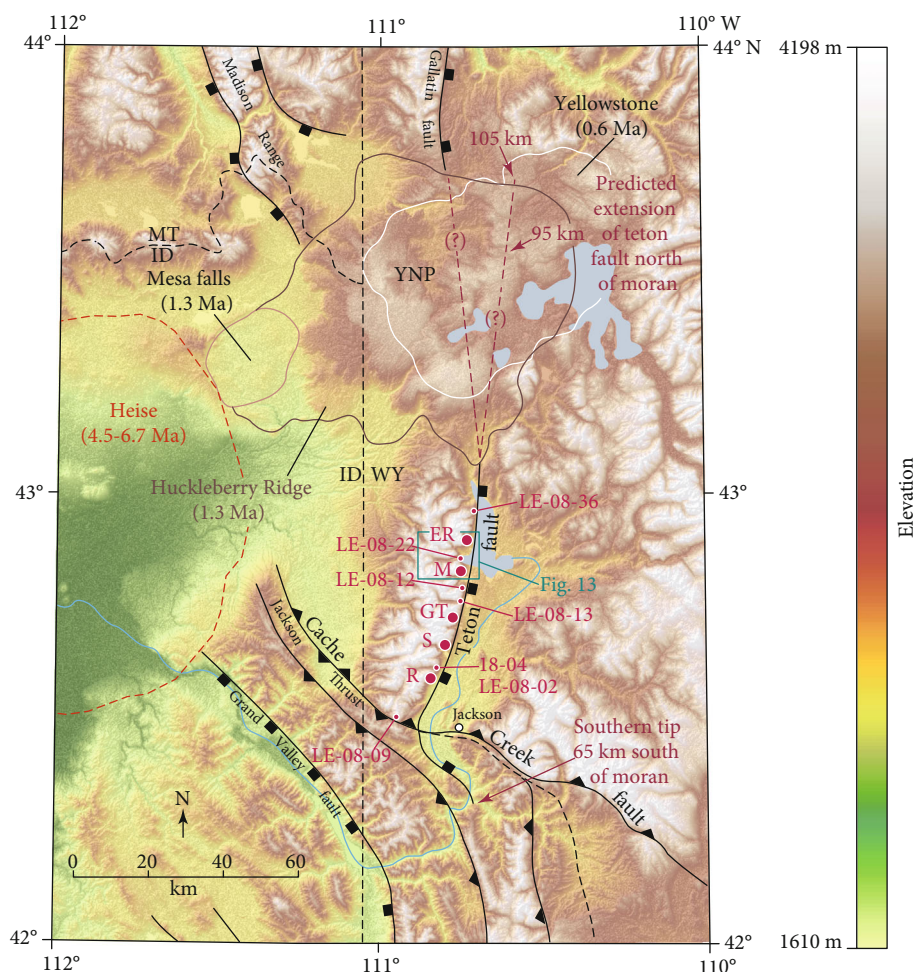
FIGURE 2: DEM map of the greater Teton-Yellowstone region, showing the position of the Teton fault, the mapped southern tip of the Teton fault near Hoback Junction, and possible northern projections of a paleo-Teton fault proposed in this study. The position of the five transects and key low elevation samples collected along strike are shown. Projections show the possible positions of a paleo-Teton fault that extended a minimum distance of 95-105 km north of Mount Moran. The conjectural linkage of the Teton fault with the Gallatin Range north of the Yellowstone hotspot is based [31], wherein the Gallatin Range was shown to have a similar uplift timing (14-16 Ma) to the Teton Range, albeit based on limited AHe data. R: Rendezvous; S: Static Peak; GT: Grand Teton; M: Moran; ER: Eagles Rest; YNP: Yellowstone National Park.

glacial till and coarse fluvial deposits, and the various criteria used to interpret offset. Despite this, most geophysical and stratigraphic studies yield maximum displacement estimates of 7-11 km [13–17], with lower estimates mostly confined to studies that examine stratigraphic tilting of Pliocene-Quaternary tuffs [12, 18, 19]. Because the latter studies focus on relatively young features, they may only record more recent increments of motion and thus yield lower displacement estimates.

The idea that the Teton fault could continue much farther north than traditionally interpreted on the basis of extent topography also has potential implications for seismic hazard evaluation. The Teton-Yellowstone region represents one of the most seismically active areas in the Intermountain US [20]. However, the Teton fault remains enigmatically quiescent and has not produced an earthquake >M_w 3.0 in recorded history [21–23]. The two most recent fault ruptures along the Teton fault were interpreted as M_w 6.8 and 7.1

events resulting from 1.3 m to 2.8 m of slip at ~4,800 and 7,900 ka, respectively [23], based on trenching studies [24–26]. If the slip rate (0.16 mm yr^{-1}) determined from those events is extrapolated to present-day, the predicted slip deficit of ~2 m suggests the Teton fault is capable of generating an M_w ~ 7.0 earthquake on known segments [12, 24–28]. However, if it can be demonstrated that the active Teton fault is much longer than previously recognized, this could have major implications for understanding fault length-related seismic hazard potential in this region (e.g., [29]).

Here, we synthesize the motion history of the Teton fault and explore the Teton Range removal hypothesis with a combination of new analyses and integration of previous datasets, including (1) new apatite (U-Th)/He (AHe) data for two new transects (Static Peak and Eagles Rest) and the upper part of the Mount Moran transect (Figure 2), which are integrated with previously reported AHe and apatite fission track (AFT) data [10]; (2) 1-D numerical models that

constrain the likely range of geothermal gradients that can influence the closure depth of AHe and AFT data; (3) development of inverse thermal history models for all transects based on the integration of new thermochronology data and geothermal gradient models; (4) integration of previously reported [30] flexural-kinematic models of crustal-scale normal fault evolution to constrain the various contributions of footwall uplift and hanging wall drop to total displacement; and (5) displacement analyses for transects based on the integration of inverse thermal history results, calculated geothermal gradients, flexural-kinematic modeling, and stratigraphic/structural relationships. Combined, these analyses allow for predictions of northern (and southern) Teton fault projections based on fault growth models, length-displacement scaling relationships, and displacement gradient analyses. Finally, we discuss possible mechanisms for removing the northern paleo-Teton Range topography and the implications that a northern fault extension may have for future seismic hazard assessments.

2. Methods

2.1. AHe and AFT Thermochronology. AHe data from two new transects collected at Static Peak and Eagles Rest Peak are here added to previously reported AHe and AFT data [10, 31, 32], which includes both multisample transects and isolated lower elevation samples collected along strike along the range front (Tables 1–6, Figure 2). Additionally, because a previous study [10] originally included multigrain aliquots in their study (i.e., multiple grains run as single aliquots) for multiple samples along the higher elevation parts of the Moran transect, new grains were separated for single-grain analysis of those samples. These new single-grain analyses are here combined with previous single-grain analyses from that same study to provide analytical consistency for input into inverse thermal history and displacement models. To make the dataset internally consistent, ages for the previously reported data [10, 31, 32] were recalculated using the same procedure in QTQt [33] that was used for calculating ages for the new data reported here. These recalculated ages rarely varied more than 1-2% from the originally reported ages. For both the new and previously reported AHe data, apatite was separated using standard gravity and magnetic techniques. For data derived from the [10] study, He was measured at Virginia Tech and U-Th were measured at the University of Arizona for single-grain aliquots. For the new analyses presented here, He and U-Th-Sm were measured for single-grain aliquots at the University of Illinois Helium Analysis Laboratory using standard techniques [34]. Each grain was outgassed via heating to 950-1050°C for three minutes using a diode laser. U, Th, and Sm abundances were analyzed using a PrismaPlus QMG 220 quadropole mass spectrometer. A minimum of six aliquots were analyzed for each new sample, although due to persistent challenges with apatite yield and quality for the Teton samples, AHe grain ages $>\pm 1\sigma$ from the mean were removed from the final mean calculation (~14% of the total aliquots run). AFT data for the Moran transect was derived directly from [10].

2.2. Inverse Thermal History Modeling. All inverse thermal history models were run using the software package QTQt v.64R5.6.0 [33], which employs a Markov chain Monte Carlo (MCMC) inversion approach. All data and parameters are reported here in accordance with the recommendations of previous methodological studies [35, 36]. AHe data inputs and grain measurements are shown in Tables 1–4. AFT data that were considered in the Moran transect are shown in Tables 5 and 6. All models include a present-day surface temperature of 4°C (average annual temperature for the Jackson Valley) and an atmospheric lapse rate of 6.5°C km^{-1}. The geothermal gradient prescribed in the QTQt models is fixed through time (fixed temperature offset) and is derived from the modeled geothermal gradient values of 25, 27, and 29°C km^{-1}, for the southern (Rendezvous), central (Static Peak and Grand), and northern (Moran and Eagles Rest) transects, respectively. Model priors were 60 ± 60 Myr for time and 70 ± 70°C for temperature, which represents the entire range of ages and closure temperatures for the AHe and AFT systems. All models included consideration of the radiation damage model [37]. AFT annealing is modeled using the multicompositional algorithms of [38, 39]. Each model was run for 10,000 burn-in iterations and 20,000 postburn-in iterations, with a uniform birth proposal distribution. Models presented are the expected T-t histories, which represent the weighted average of accepted models. The acceptance rates for each model are included in Figures 3 and 4. For a complete treatment of the MCMC inversion approach employed by QTQT, the reader is referred to [33]. The comparison between modeled and observed ages, which are essential for evaluating the validity of inverse model results, are included for each model (Figures 3 and 4).

2.3. Geothermal Gradient Modeling. Because the models presented here must include a necessary dependency on the observed or assumed thermal structure of the upper crust (~15 km), it is useful to consider any available constraints on these modeling variables, particularly because the thermal structure of the lithosphere in the Teton-Yellowstone region is complex, owing to migration of the Yellowstone hotspot. In the continental crust, the geothermal gradient is controlled by the mantle heat flow (Q_m) into the base of the crust, the internal radiogenic heat production (A), and thermal conductivity (K) of the crust, the surface heat flow (Q_o), and any advectionary heat transport processes.

Depth filtered P-wave seismic inversion shows that, despite being immediately adjacent to the Yellowstone hotspot, the Teton Range is underlain by a relatively fast P-wave velocity zone from 2 to 14 km depth, likely indicating a zone of relatively cold crust adjacent to the low-velocity partial melt zones beneath the present-day caldera [40]. Because the modern Teton Range appears to be underlain by relatively cold crust despite being as close to the Yellowstone hotspot as at any point in its history, we assume in our models that the present-day geothermal gradient represents the maximum geothermal gradient experienced by these rocks in the timeframe being considered (>50 Ma-

TABLE 1: Southern and along-strike (LE) Teton Range AHe data of Brown et al. (2017) and Swallom (2019). Rendezvous data used as input for inverse thermal history modeling. In all samples with the 08 prefix, Sm was not measured.

Sample	Lat.	Lon.	Elev. (m)	L (μm)	W (μm)	He (nmol/g)	U (ppm)	Th (ppm)	Sm (ppm)	Raw age (Ma)	Error (Ma)	Corr. age (Ma)	Ave. age (Ma)	Std. dev (Ma)
Teton Pass														
LE-08-09-1	43.4999	-110.9387	2481	110	91	8.1454545	26.5	16.4	n/a	49.55	3.96	70.43	73.67	4.58
LE-08-09-4				103	98	20.9701493	56.2	62.9	n/a	54.50	4.36	76.91		
Rendezvous														
R1-08-19-A	43.5983	-110.8603	2728	110	83	36.0897436	122.3	143.2	n/a	42.72	3.42	62.89	67.99	4.74
R1-08-19-B				96	100	28.8831169	83.9	131.9	n/a	46.37	3.71	66.36		
R1-08-19-C				119	95	62.0917431	179.1	235.5	n/a	48.87	3.91	68.49		
R1-08-19-D				125	100	42.8015873	113.3	139.9	n/a	54.01	4.32	74.20		
R2-08-27-B	43.5900	-110.8489	2400	161	121	5.0102564	24.3	17.2	n/a	32.68	2.62	41.84	46.26	3.93
R2-08-27-C				154	114	7.8545455	32.0	40.8	n/a	34.88	2.79	45.47		
R2-08-27-D				147	87	5.1157025	21.6	17.8	n/a	36.66	2.93	51.37		
R2-08-27-1				138	92	9.0566440	39.8	44.1	n/a	33.36	2.67	46.37		
R3-08-28-2	43.5873	-110.8468	2201	89	100	1.0188679	34.6	3.6	n/a	5.33	0.43	7.65	7.62	1.57
R3-08-28-3				156	108	2.1052632	49.4	11.9	n/a	7.47	0.60	9.78		
R3-08-28-4				104	92	0.5660377	23.9	1.6	n/a	4.32	0.35	6.12		
R3-08-28-5				74	62	1.0000000	43.8	11.2	n/a	3.99	0.32	6.93		
Granite														
18-04-03	43.6165	-110.8523	2383	180	133	135.4443022	383.0	592.7	72.4	47.83	3.83	59.99	58.77	5.56
18-04-04*				125	102	35.2244022	127.0	76.8	115.4	44.82	3.59	60.89		
18-04-05				158	85	16.8797001	79.7	25.0	137.7	36.41	2.91	50.72		
18-04-06				191	108	34.3859331	107.4	95.1	53.9	48.89	3.91	63.47		
LE-08-02-1	43.6156	-110.8161	2066	138	115	1.8474576	37.5	4.2	n/a	8.90	0.71	11.59	8.99	2.57
LE-08-02-2				239	110	1.0000000	35.5	3.6	n/a	5.10	0.41	6.46		
LE-08-02-8				138	92	3.4545455	93.3	23.8	n/a	6.47	0.52	8.91		
Cascade														
LE-08-13-A	43.7659	-110.7456	2088	113	62	1.3142857	40.7	10.4	n/a	5.64	0.45	9.16	10.93	1.56
LE-08-13-B				98	58	6.9393939	169.8	52.2	n/a	7.06	0.57	12.10		
LE-08-13-C				97	74	1.8412698	43.1	10.3	n/a	7.49	0.60	11.52		
Rockchuck														
LE-08-12-4	43.7898	-110.7413	2230	147	110	0.1666667	5.6	7.5	n/a	4.19	0.34	5.54	7.32	2.52
LE-08-12-7				87	83	3.9230769	105.0	66.6	n/a	6.02	0.48	9.10		
Moran Bay														
LE-08-22-A	43.8603	-110.7707	2188	101	64	1.7380952	48.5	13.7	n/a	6.23	0.50	10.12	10.16	1.21
LE-08-22-B				144	56	2.8648649	70.2	18.0	n/a	7.13	0.57	11.84		

TABLE 1: Continued.

Sample	Lat.	Lon.	Elev. (m)	L (μm)	W (μm)	He (nmol/g)	U (ppm)	Th (ppm)	Sm (ppm)	Raw age (Ma)	Error (Ma)	Corr. age (Ma)	Ave. age (Ma)	Std. dev (Ma)
LE-08-22-C				93	71	2.8378378	79.4	25.2	n/a	6.16	0.49	9.70		
LE-08-22-D				101	76	2.1029412	61.3	18.6	n/a	5.93	0.48	8.99		
Colter														
LE-08-36-4	43.9487	-110.7055	2108	69	64	0.3333333	4.3	4.7	n/a	11.41	0.91	20.19	15.94	6.71
LE-08-36-5				83	64	3.3809524	73.5	12.3	n/a	8.20	0.66	8.20		
LE-08-36-7				74	55	0.1666667	2.7	1.1	n/a	10.44	0.84	19.43		

Grains marked with an * indicate grains modeled with only one euhedral termination (1 T). All others modeled as 2 T. *L*: length; *W*: width. Granite Ca.: Granite Canyon.

TABLE 2: Central Teton Range AHe data for the Static Peak transect. Data are used as inputs for inverse thermal history modeling of the Static Peak transect.

Sample	Lat.	Lon.	Elev. (m)	L (μm)	W (μm)	He (nmol/g)	U (ppm)	Th (ppm)	Sm (ppm)	Raw age (Ma)	Error (Ma)	Corr. age (Ma)	Ave. age (Ma)	Std dev (Ma)
Static														
S1-18-02-1	43.6828	-110.8163	3446	114	77	64.8085952	100.5	256.7	122.8	74.07	5.93	112.87	105.77	6.88
S1-18-02-3				135	72	49.9683126	77.7	230.4	98.7	69.67	5.57	107.17		
S1-18-02-4				149	60	164.9287648	289.9	763.8	221.5	64.64	5.17	106.71		
S1-18-02-5				93	74	44.7696454	88.6	202.0	88.7	60.60	4.85	96.34		
S2-18-03-2*	43.6771	-110.8125	3035	134	64	276.9067622	1018.6	313.7	177.7	46.83	3.75	73.53	62.98	8.23
S2-18-03-3				121	93	45.2189680	209.1	19.7	192.4	39.07	3.13	54.22		
S2-18-03-5*				167	85	175.5124956	596.3	434.1	282.1	46.38	3.71	64.68		
S2-18-03-6				172	110	42.9827920	166.4	26.0	190.6	46.01	3.68	59.48		
S3-18-05-3*	43.6742	-110.8045	2875	147	74	25.0026812	113.2	10.7	1647.7	39.27	3.14	57.26	59.36	3.68
S3-18-05-5				129	97	38.0028214	160.3	13.5	2766.3	42.11	3.37	57.22		
S3-18-05-6				136	85	54.2785921	213.2	22.5	2556.6	45.29	3.62	63.61		
S4-18-06-2	43.6718	-110.7994	2696	186	151	3.5224854	27.2	6.6	101.0	22.59	1.81	27.44	33.20	4.54
S4-18-06-3				186	129	1.7781872	12.2	2.6	61.7	25.54	2.04	31.83		
S4-18-06-5				211	148	2.3760321	13.0	4.5	69.0	31.08	2.49	37.61		
S4-18-06-6				184	136	2.2316362	13.4	3.1	68.1	29.06	2.33	35.91		
S6-18-01-1	43.6584	-110.8191	2267	202	127	0.4697099	5.0	3.3	97.9	14.75	1.18	18.38	21.78	4.73
S6-18-01-3				169	127	4.0812575	29.8	16.0	303.8	22.26	1.78	28.06		
S6-18-01-5				201	148	1.3916206	14.3	12.8	168.8	14.70	1.18	17.90		
S6-18-01-6				181	128	1.5540928	14.0	6.5	225.5	18.20	1.46	22.77		
S7-08-11C	43.6479	-110.8074	2060	230	110	0.1964286	3.5	8.4	n/a	6.63	0.53	8.55	11.84	2.98
S7-08-11D				193	166	0.1370968	1.5	3.6	n/a	10.80	0.86	13.05		
S7-08-11G				193	138	2.1891892	31.4	7.3	n/a	12.25	0.98	15.06		
S7-08-11H				221	156	4.5871560	124.7	11.1	n/a	6.68	0.53	7.99		
S7-08-11-02				101	83	2.9411765	48.2	32	n/a	9.77	0.78	14.45		
S7-08-11-05				92	64	5.1250000	127.5	14.5	n/a	7.25	0.58	11.91		

Grains marked with an * were modeled with only one euhedral termination (1 T). All others modeled as (2 T).

TABLE 3: Central and northern Teton Range AHe data of Brown et al. (2017) for the Grand transect and Hoar (2018) for the Eagles Rest transect. Data are used as input for inverse thermal history modeling of the Grand and Eagles Rest transects.

Sample	Lat.	Lon.	Elev. (m)	L (μm)	W (μm)	He (nmol/g)	U (ppm)	Th (ppm)	Sm (ppm)	Raw age (Ma)	Error (Ma)	Corr. age (Ma)	Ave. age (Ma)	Std dev (Ma)
Grand														
G1-08-24-1	43.7409	-110.8046	4040	87	64	3.8571429	19.7	8.4	n/a	32.91	2.63	54.90	49.54	3.42
G1-08-24-4				113	55	2.5714286	15.6	4.7	n/a	28.49	2.28	49.17		
G1-08-24-5				115	51	3.3333333	23.3	7.8	n/a	24.55	1.96	44.22		
G1-08-24-6				115	51	4.0000000	23.8	14.3	n/a	27.24	2.18	49.39		
G1-08-24-7				97	46	2.5000000	17.6	4.4	n/a	24.84	1.99	49.07		
G1-08-24-8				110	55	4.2857143	23.5	16.8	n/a	28.88	2.31	50.50		
G4-TT5-5	43.7260	-110.7910	2853	212	129	0.0125000	15.1	1.1	n/a	22.22	0.8200	27.10	25.75	5.42
G4-TT5-6				230	101	0.0139000	25.7	2.9	n/a	21.18	0.7700	27.50		
G4-TT5-8				138	92	0.0025000	12.9	0.0	n/a	16.62	0.7730	21.50		
G4-TT5-9				138	92	0.0042000	20.3	0.0	n/a	16.65	0.7400	22.50		
G4-TT5-21				101	74	0.0008000	12.3	1.2	n/a	11.29	0.6800	16.60		
G4-TT5-22				166	64	0.0013000	11.0	1.0	n/a	16.13	0.6300	25.60		
G4-TT5-23				120	64	0.0032000	31.2	4.6	n/a	19.24	0.6500	29.60		
G4-TT5-24				110	64	0.0010000	15.0	0.0	n/a	13.18	0.6400	20.60		
G4-TT5-25				202	64	0.0031000	22.3	0.9	n/a	15.68	0.6400	24.50		
G5-TT8-1	43.7237	-110.7639	2461	81	76	0.0036000	28.2	11.3	n/a	5.33	0.7000	7.62	11.31	5.22
G5-TT8-2				92	75	0.0489000	48.1	7.1	n/a	11.55	0.7700	15.00		
G6-08-23-A	43.7388	-110.7484	2130	142	81	0.0219000	58.3	13.4	n/a	5.96	0.8383	7.11	6.81	0.37
G6-08-23-B				131	90	0.0133000	41.8	6.9	n/a	5.21	0.8296	6.28		
G6-08-23-C				115	67	0.0060000	37.1	5.9	n/a	5.46	0.7994	6.83		
G6-08-23-D				167	116	0.0235000	29.4	3.1	n/a	6.03	0.8578	7.03		
Eagles Rest														
E1-17-09-03	43.8983	-110.7495	3120	109	83	15.4899238	43.2	7.3	93.3	63.48	5.08	92.25	92.25	0.00
E2-17-10-04	43.8989	-110.7467	2972	79	61	18.8886488	74.1	9.7	89.5	45.65	3.65	78.70	78.96	2.95
E2-17-10-05				113	70	11.9929958	42.3	6.8	91.2	50.35	4.03	77.53		
E2-17-10-07				85	60	22.3970883	91.0	6.1	225.8	44.66	3.57	76.44		
E2-17-10-08				60	49	23.5168314	104.4	22.2	142.7	39.61	3.17	83.16		
E4-17-12-02	43.9021	-110.7375	2607	104	67	0.2728826	14.2	1.7	35.4	3.45	0.28	5.45	7.05	1.15
E4-17-12-04				77	50	0.3367883	14.4	7.1	22.6	3.87	0.31	7.60		
E4-17-12-06				126	65	0.2828641	11.0	2.5	28.5	4.51	0.36	7.06		
E4-17-12-07				72	50	0.3262072	13.4	6.0	22.5	4.07	0.33	8.09		

Grains marked with an * were modeled with only one euhedral termination (1 T). All others modeled as (2 T).

TABLE 4: Northern Teton Range AHe data of Brown et al. (2017) and this study for the Moran transect. Data are used as inputs for inverse thermal history modeling of the Moran transect.

Sample	Lat.	Lon.	Elev. (m)	L (μm)	W (μm)	He (nmol/g)	U (ppm)	Th (ppm)	Sm (ppm)	Raw age (Ma)	Error (Ma)	Corr. age (Ma)	Ave. age (Ma)	Std dev (Ma)
Moran														
M1-08-15-1	43.8339	-110.7764	3835	106	55	2.9230769	37.2	21.0	n/a	12.85	1.03	22.51	23.02	2.91
M1-08-15-2*				129	58	2.2988506	34.1	7.4	n/a	11.89	0.95	19.59		
M1-08-15-4*				129	55	2.1518987	25.2	0.0	n/a	15.81	1.27	26.66		
M1-08-15-8*				106	69	2.1782178	26.5	2.0	n/a	14.97	1.20	23.30		
M2-08-30-03	43.8318	-110.7723	3505	160	79	1.2325581	12.5	8.5	n/a	15.74	1.26	22.53	22.75	4.82
M2-08-30-04				88	81	0.8305085	9.7	2.8	n/a	14.85	1.19	22.46		
M2-08-30-1N				150	89	3.3736728	26.9	13.8	361.6	20.39	1.63	28.16		
M2-08-30-2N				124	76	2.3335789	37.9	18.8	446.7	10.06	0.81	14.89		
M2-08-30-3N				100	81	7.4414834	91.0	20.7	1042.7	14.19	1.14	20.99		
M2-08-30-6 N				90	70	3.9644763	36.7	22.0	574.8	17.22	1.38	27.44		
M3-08-31A*	43.8300	-110.7694	3304	115	72	1.1600000	14.7	17.2	n/a	11.45	0.92	17.65	15.30	6.81
M3-08-31D				112	82	1.2333333	26.8	16.5	n/a	7.44	0.596	10.90		
M3-08-31E				110	74	0.8304581	20.3	20.4	n/a	6.12	0.49	9.37		
M3-08-31-01N				101	73	8.7867525	78.9	76.0	75.5	16.80	1.34	26.13		
M3-08-31-03N				137	113	2.7207553	42.6	45.9	28.3	9.42	0.75	12.44		
M4-08-03A	43.8265	-110.7661	2975	93	63	1.1794872	21.0	7.7	n/a	9.58	0.77	15.91	14.79	3.21
M4-08-03B				88	64	1.0000000	15.0	6.1	n/a	11.27	0.90	18.76		
M4-08-03-2				120	92	0.9812182	18.7	3.8	n/a	9.28	0.74	12.95		
M4-08-03-4				101	78	0.3210025	7.2	2.3	n/a	7.68	0.61	11.54		
M5-08-05-2	43.8244	-110.7593	2636	101	78	2.2105263	51.0	1.4	n/a	7.98	0.64	11.94	11.94	0.00
M6-08-06-1	43.8222	-110.7563	2450	92	64	0.7500000	23.8	35.3	n/a	4.32	0.35	7.27	7.52	2.22
M6-08-06-4				138	115	3.5454545	62.1	95.6	n/a	7.75	0.62	10.22		
M6-08-06-5				74	92	0.5714286	18.8	4.0	n/a	5.36	0.43	8.01		
M6-08-06-6				170	156	0.3863636	20.1	5.5	n/a	3.34	0.27	4.07		
M6-08-06-10				83	69	1.1338521	16.9	119.0	n/a	4.66	0.37	8.01		
M7-08-07A	43.8192	-110.7526	2185	105	79	2.8676471	70.2	42.6	n/a	6.62	0.53	9.90	10.13	1.61
M7-08-07C				114	83	2.2835821	63.3	33.3	n/a	5.95	0.48	8.65		
M7-08-07D				95	78	4.0576923	83.3	56.8	n/a	7.77	0.62	11.85		
M8-08-32B	43.8173	110.7531	2116	148	63	1.5744681	66.5	28.2	n/a	3.98	0.32	6.25	8.70	1.83
M8-08-32D				107	67	1.1600000	34.8	9.4	n/a	5.81	0.47	9.17		
M8-08-32-1				106	69	0.6901709	23.1	3.2	n/a	5.36	0.43	8.36		
M8-08-32-2				97	87	1.7499103	40.0	6.9	n/a	7.79	0.62	11.34		
M8-08-32-3				124	69	0.6719124	22.0	3.2	n/a	5.47	0.44	8.37		

Grains marked with an * were modeled with only one euhedral termination (1 T). All others modeled as (2 T).

TABLE 5: Spontaneous (N_s) and induced (N_i) apatite fission track counts and Dpar compositional values for samples TR-08-15, TR-08-03, and TR-08-32 from the Mount Moran transect. Zeta calibration factor (ζ) = 315.4 ± 13.2, ρ_d = 1449800 for TR-08-15, ρ_d = 1499450 for TR-08-03, ρ_d = 1338080 for TR-08-32, and N_d = 4262 for all three samples. Track count and length data were used as inputs for the inverse thermal history model of the Moran transect. Calculated central ages input into inverse thermal history models are 37.99 ± 2.63 Ma (TR-08-15), 13.62 ± 1.88 Ma (TR-08-03), and 11.70 ± 1.62 Ma (TR-08-32).

TR-08-15			TR-08-03			TR-08-32		
N_s	N_i	Dpar	N_s	N_i	Dpar	N_s	N_i	Comp
4	31	1.5	8	87	1.6	4	19	36
11	37	1.5	2	35	1.4	1	29	28
12	117	1.6	2	44	1.5	2	38	60
15	69	1.6	1	45	1.3	6	109	50
6	54	1.6	0	13	1.5	2	49	60
6	65	1.6	1	17	1.0	4	62	50
7	44	1.9	2	15	1.4	4	49	50
19	66	1.4	3	19	1.7	3	47	60
37	222	1.7	4	57	1.7	1	29	60
22	148	1.8	3	88	1.2	1	48	50
17	96	1.8	2	38	1.5	2	25	50
8	71	1.7	1	20	1.3	0	15	50
3	26	2.1	1	30	1.5	5	34	60
9	59	1.4	3	41	1.4	4	90	50
6	42	1.4	2	63	1.4	3	63	70
10	61	1.6	1	35	1.3	8	137	60
21	105	1.6	2	49	1.1	1	49	50
27	116	1.8	5	47	0.9	1	31	60
16	100	1.7	8	133	1.4	1	30	36
2	19	1.7	1	16	1.8	3	56	50

present). These P-wave tomographic models agree closely with previous work [41], which showed a present-day geothermal gradient of 18-27°C for Teton region. Here, the measured surface heat flow values (Figure 5) [42] are used as constraints, and mantle heat flow and radiogenic heat production are varied to derive a range of possible geothermal gradients for the Teton Range. The range of steady-state geotherms is calculated by solving the heat conduction equation with a contribution of radiogenic heat production:

$$T(y) = T_o + \frac{Q_o}{K}y + \frac{A}{2K}y^2, \tag{1}$$

where T is temperature for a given depth (y), T_o is surface temperature, and Q_o is the surface heat flow. In the geothermal gradient models presented here, heat advection is not considered, as thermal-kinematic models of Teton uplift scenarios by [30] showed minimal advectionary heat transport and yield geothermal gradients of 20-27°C km^{-1} for the upper 10 km of the crust. Here, the geothermal gradient is constrained using surface heat flow values of 0.075, 0.081, and 0.087 W m^{-2} for the southern, central, and northern Tetons, respectively [42]. By using fixed Q_o values for geothermal gradient calculations, the range of possible Q_m and A values can be explored, and those values for each model are shown in Table 7. Although there are multiple methods for characterizing the distribution of radiogenic heat pro-

duction (A) in the crust, including layered and exponential models, it is here modeled as a constant average value throughout the entire 30 km crustal thickness. Two-dimensional thermal-kinematic models of [30] that include exponential models of heat production in the crust still yield near surface (<10 km) geothermal gradients of 20-27°C km^{-1}, similar to modern geothermal gradients calculated by [41].

2.4. Flexural-Kinematic Modeling. Flexural-kinematic models [30] are included here to evaluate how a range of subsurface geometries for the Teton fault and the effective elastic thickness of the crust in the region could influence the footwall isostatic response during fault displacement. To constrain the range of viable geometries and crustal parameters, the topographic profiles of each model result were compared to east-west swath topographic profiles from the Gros Ventre uplift across the Teton Range near Mount Moran to the Teton Basin west of the range. Swath profiles were produced using the Swath Profiler ArcGIS add-in [43] and a 10 m DEM. The swath was aligned through Mount Moran, which was identified as the locus of maximum displacement [10]. The SwathProfiler calculates a maximum, minimum, and mean elevation profile based on topographic profiles of 50 equally spaced transects within the 6 km swath width, and these calculated profiles can then be compared with topographic profiles produced by various iterations of the flexural-kinematic model. These comparisons were then

TABLE 6: Apatite fission track lengths, measured angles from the *c*-axis, and Dpar compositional values for samples TR-08-15 and TR-08-03 from the Mount Moran transect. Track count and length data were used as inputs for the Moran inverse thermal history model. No track length data were collected for TR-08-32.

TR-08-15			TR-08-15			TR-08-03		
Length (µm)	Angle (°)	Dpar	Length (µm)	Angle (°)	Dpar	Length (µm)	Angle (°)	Dpar
13.2	75.8	1.3	9.8	69.6	1.4	14.3	67.7	1.4
13.2	75.8	1.3	9.8	80.8	1.6	11.7	40.8	1.9
11.3	46.5	1.3	12.6	32.1	1.6	14.9	41.1	1.8
7.6	78.0	1.7	10.2	85.8	1.9	10.4	72.9	1.8
14.4	87.1	1.3	9.7	58.3	1.9	7.3	70.8	1.7
10.1	64.1	1.8	10.9	89.5	1.9	12.2	57.6	1.7
9.4	3.0	1.7	14.8	51.6	1.9	15.0	57.5	1.4
12.2	89.7	1.3	11.9	44.8	1.9	11.8	39.4	1.5
11.6	38.7	1.5	11.7	46.0	1.9	13.9	24.0	1.9
11.8	33.2	1.6	8.5	54.2	1.8	9.9	38.1	1.7
10.5	58.7	1.5	13.2	39.5	1.8	12.8	54.2	1.7
11.0	49.1	1.3	10.2	4.0	1.8	12.9	84.7	1.5
13.4	45.4	1.3	13.7	47.6	1.8	11.7	53.8	1.6
12.6	44.1	1.3	14.2	64.4	1.5	11.1	88.0	1.3
12.5	75.4	1.3	9.5	43.1	1.9	11.5	63.8	1.4
13.1	47.8	1.3	11.9	38.9	1.9	13.6	62.2	1.4
8.4	55.8	1.7	15.3	27.6	1.7	14.8	58.3	1.5
8.7	41.5	1.7	13.8	25.1	2.0	12.3	88.5	1.5
11.5	45.1	1.7	9.1	30.3	2.0	15.7	90.0	1.4
9.7	37.6	1.7	14.1	70.6	1.4	8.1	55.6	1.9
11.6	75.7	1.7	12.6	43.4	1.4	11.2	46.4	0.7
10.0	68.5	1.7	14.6	37.6	1.4	14.4	50.5	1.3
12.2	48.9	1.7	14.3	70.2	1.4	14.9	57.8	1.5
9.4	72.6	1.7	7.1	73.0	1.9	10.0	27.2	1.3
13.4	72.7	1.7	12.6	76.3	1.5	12.4	1.6	1.1
10.2	27.4	1.7	12.5	47.0	1.7	14.4	32.2	1.1
9.9	34.7	1.7	11.5	10.5	1.7	13.4	33.4	1.3
12.0	72.8	1.7	9.0	51.8	1.5	13.4	48.4	1.5
11.4	68.5	1.5	9.5	21.6	1.5	12.5	56.1	1.1
13.1	67.6	1.5	9.8	55.7	1.6			
15.0	22.9	1.5	8.1	44.0	1.6			
10.2	63.2	1.7	15.2	34.7	1.7			
11.1	78.2	1.3	12.8	37.9	1.7			
10.4	26.7	2.0	14.3	72.4	2.6			
12.4	71.5	1.6	11.8	89.2	2.6			
12.1	85.8	1.6	13.8	46.4	2.0			
12.0	60.8	1.6	8.8	40.3	1.4			
13.5	33.2	1.5	15.2	80.0	1.7			
12.3	69.8	1.6	13.3	57.9	1.5			
13.5	79.0	1.8	13.3	60.7	1.9			
15.5	22.6	1.9	11.3	67.6	1.6			
11.3	86.5	1.9	12.8	23.4	1.6			
11.8	75.8	1.9						
12.1	76.6	1.9						
10.0	72.3	1.7						
10.7	48.9	1.8						

TABLE 6: Continued.

TR-08-15			TR-08-15			TR-08-03		
Length (μm)	Angle (°)	Dpar	Length (μm)	Angle (°)	Dpar	Length (μm)	Angle (°)	Dpar
10.0	46.7	1.8						
11.1	31.4	1.9						
14.3	45.4	1.6						
15.6	70.6	1.5						
9.8	63.3	1.5						
11.3	50.2	1.8						
10.8	75.7	1.6						
13.7	35.9	1.6						
11.4	65.8	1.6						
10.3	36.3	1.6						
13.2	65.6	1.8						
11.8	72.6	1.7						

used to select a reference case for modeling the various contributions of footwall uplift and hanging wall drop to the total displacement. The details of this methodology and the results of all models are described in [30]. Initial flexural-kinematic models included near-surface fault dips ranging from 45-70°, listric detachment depths of 15-20 km, and effective elastic thickness (T_e) values of 5, 10, and 15 km, based on interpretations from multiple studies of Basin and Range normal faults [44–46]. Footwall erosion was not included in the simple model presented here, but [30] considered incremental footwall erosion following each displacement step that yields the range of total eroded thickness interpreted in this system. Additionally, the models of [30] included ongoing sedimentation in the modeled hanging wall to match that observed in the Jackson Hole basin. Those models of [30] yield similar results as our simple model included here. Flexural-kinematic modeling was completed using Move from Petroleum Experts. The flexural-isostatic response in Move is described by the equation for a continuous 2D beam [47]:

$$q = D \frac{d^4 w}{dx^4} + (\rho_m - \rho_c) g \, w, \qquad (2)$$

where applied vertical load (q) required to produce a deflection ($w(x)$) is a function of the flexural rigidity (D). In this equation, ρ_m is mantle density (3300 kg m^{-3}), ρ_c is the density of the removed crustal material (2750 kg m^{-3}), and g is the acceleration of gravity (9.81 m s^{-2}). Flexural rigidity (D) of the lithosphere is

$$D = \frac{E \, T_e^3}{12 \, (1 - \nu^2)}, \qquad (3)$$

where E is Young's modulus, T_e is effective elastic thickness, and ν is Poisson's ratio. Only the simple reference case model (near-surface fault dip = 70°, listric detachment depth = 15 km, T_e = 5 km) determined by [30] is considered here.

3. Results

3.1. Thermochronology and Inverse Thermal History Modeling.
All analytical results are shown in Tables 1–6. As expected, AHe ages generally increase with increasing elevation along each transect; however, the age elevation gradients are highly varied between the five transects (Figure 6). The Moran transect yields the steepest age-elevation gradient. In the southern and central Teton Range, inverse thermal history models of the Rendezvous, Static Peak, and Grand Teton transects yield periods of relatively rapid Miocene to present cooling with onset ages of ~8 Ma, ~15 Ma, and ~9 Ma, respectively (Figure 3). Inverse thermal history models of the Moran and Eagles Rest transects in the northern Teton Range yield a similar footwall cooling event with onset ages of 10-8 Ma (Figure 4). With the exception of the Eagles Rest transect, inverse thermal history models of the other four transects also yield an earlier Eocene-Miocene cooling event; however, the expected T-t histories show a substantial variation in age for the earlier cooling event(s). The expected model for the Rendezvous, Static Peak, Grand, and Moran transects yield Eocene-Miocene cooling events of 48-41 Ma, 31-23 Ma, 50-26 Ma, and 25-19 Ma, respectively, and the expected model for the Moran transect also yields a separate cooling event at 61-40 Ma. However, the credible intervals increase substantially for the earlier cooling histories predicted in the Rendezvous (48-41 Ma) and Grand (31-23 Ma) transects. The Static Peak and Moran (50-26 Ma, 61-40 Ma) inverse thermal history models show narrower credible intervals for the earlier cooling event at 31-23 Ma and 25-19 Ma, respectively, and this is addressed in the discussion.

3.2. Geothermal Gradient Modeling.
Twelve separate models encompassing the likely range of present-day Teton region geothermal gradients were produced (Figure 7). Models are separated into three groups representing surface heat flow values (Q_o) of 0.075, 0.081, and 0.087 W m^{-2} that match the observed conditions in the southern, central, and northern Teton Range, respectively [42] (Figure 5). Despite the
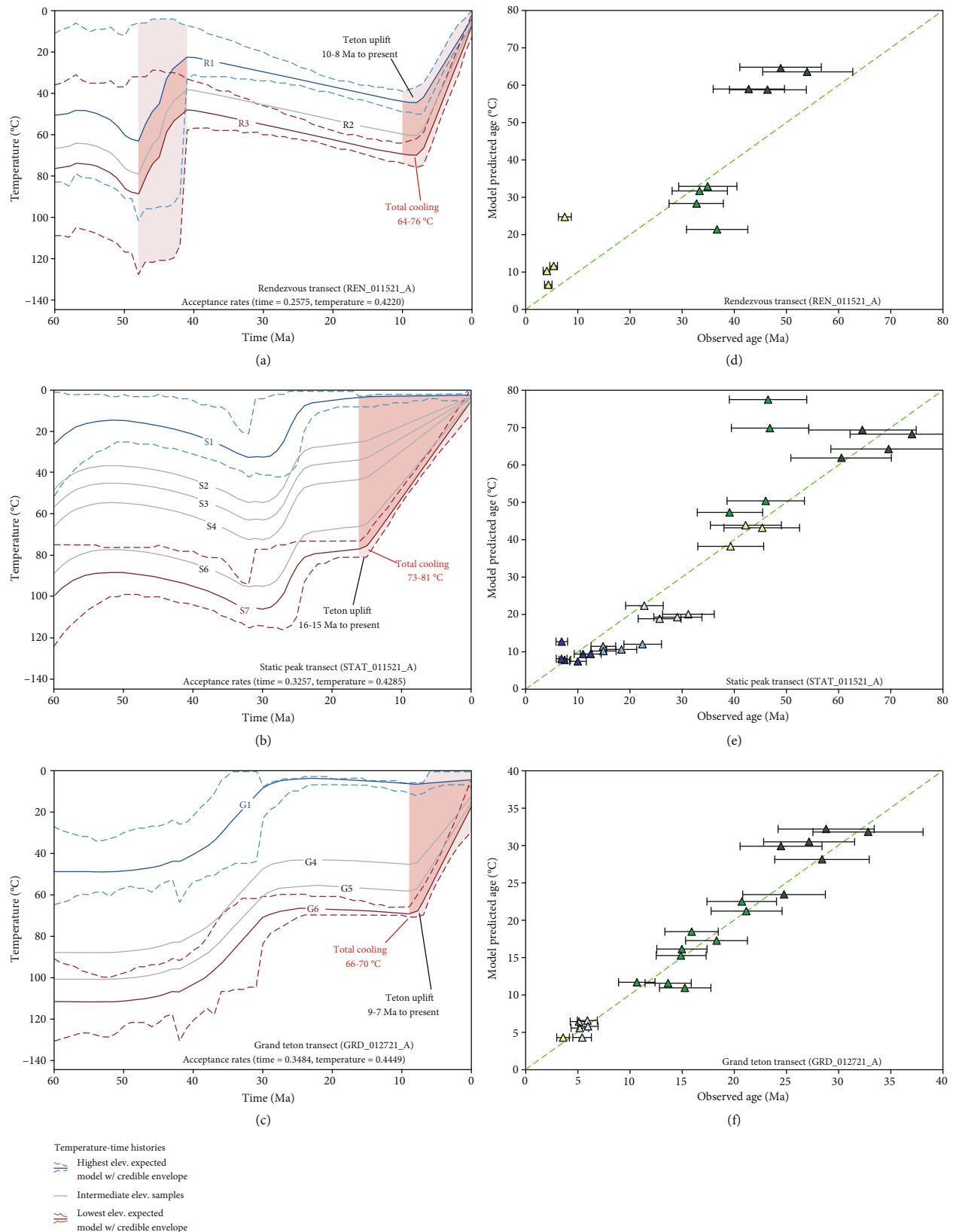
FIGURE 3: QTQt inverse thermal history models for the (a) Rendezvous, (b) Static Peak, and (c) Grand Teton transects. The most recent onset of rapid cooling interpreted to reflect onset of Teton faulting and uplift of the Teton Range, shown in pink. (d–f) Comparison of observed ages vs. modeled predictions (QTQt expected model) for base case models. Individual samples included in the Rendezvous (R1-R3), Static Peak (S1-S4, S6, S7), and Grand Teton (G1, G4-G6) models correspond to sample numbers shown in Tables 1–3, respectively.

(a)

(c)

(b)

(d)
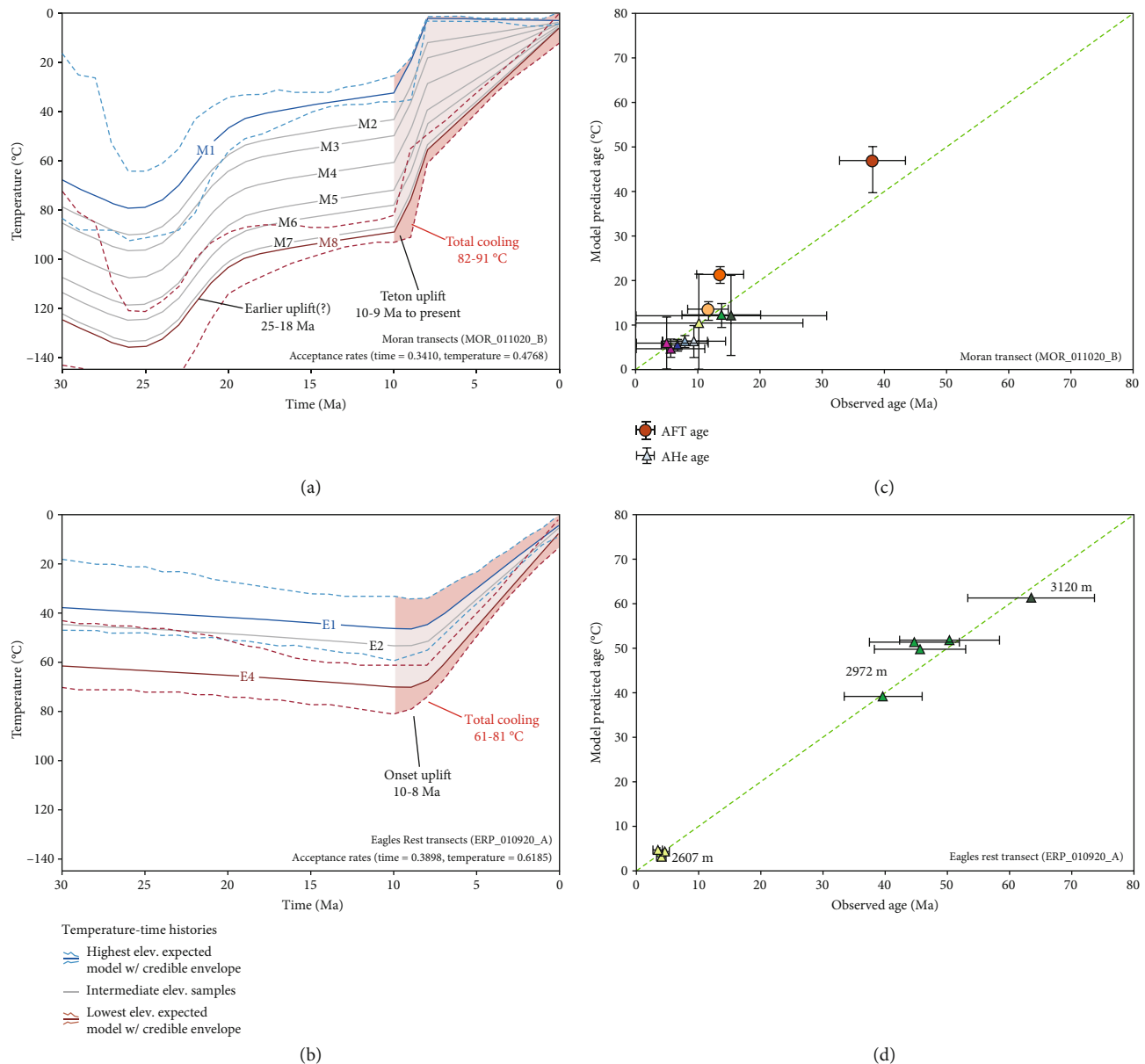
FIGURE 4: QTQt inverse thermal history models for the (a) Moran and (b) Eagles Rest transects. The most recent onset of rapid cooling interpreted to reflect onset of Teton faulting and uplift of the Teton Range, shown in pink. (c, d) Comparison of observed ages vs. modeled predictions (QTQt expected model) for base case models. Individual samples included in the Moran (M1-M8) and Eagles Rest (E1, E2, E4) models correspond to sample numbers shown in Table 3.

incorporation of a range of mantle heat flow (Q_m) and radiogenic heat production (A) values, models yield a relatively small range of geothermal gradient values for the upper 5 km of the crust. Gradients ranged from 22 to 25°C km^{-1}, 24 to 27°C km^{-1}, and 26 to 29°C km^{-1} for the southern, central, and northern Teton Range, respectively. In order to produce the most conservative values for footwall exhumation to be interpreted from the cooling history, the maximum modeled geothermal gradient for each region was used for inverse thermal history models and footwall cooling calculations.

3.3. Flexural-Kinematic Modeling.

The flexural-kinematic response of the modeled Teton Range to the entire range of parameters is reported in [30]. Here, we only report the results from displacement studies of the base case model (near-surface fault dip = 70°, T_e = 5 km, Z_d = 15 km) that produced the closest match between the modeled and observed flexural-topographic profile (Figure 8). In the flexural-kinematic model, footwall uplift increases with increasing displacement (Figure 9), with the footwall uplift contribution to total displacement decreasing from ~35% to ~23% as total displacement increases from 2 to 20 km
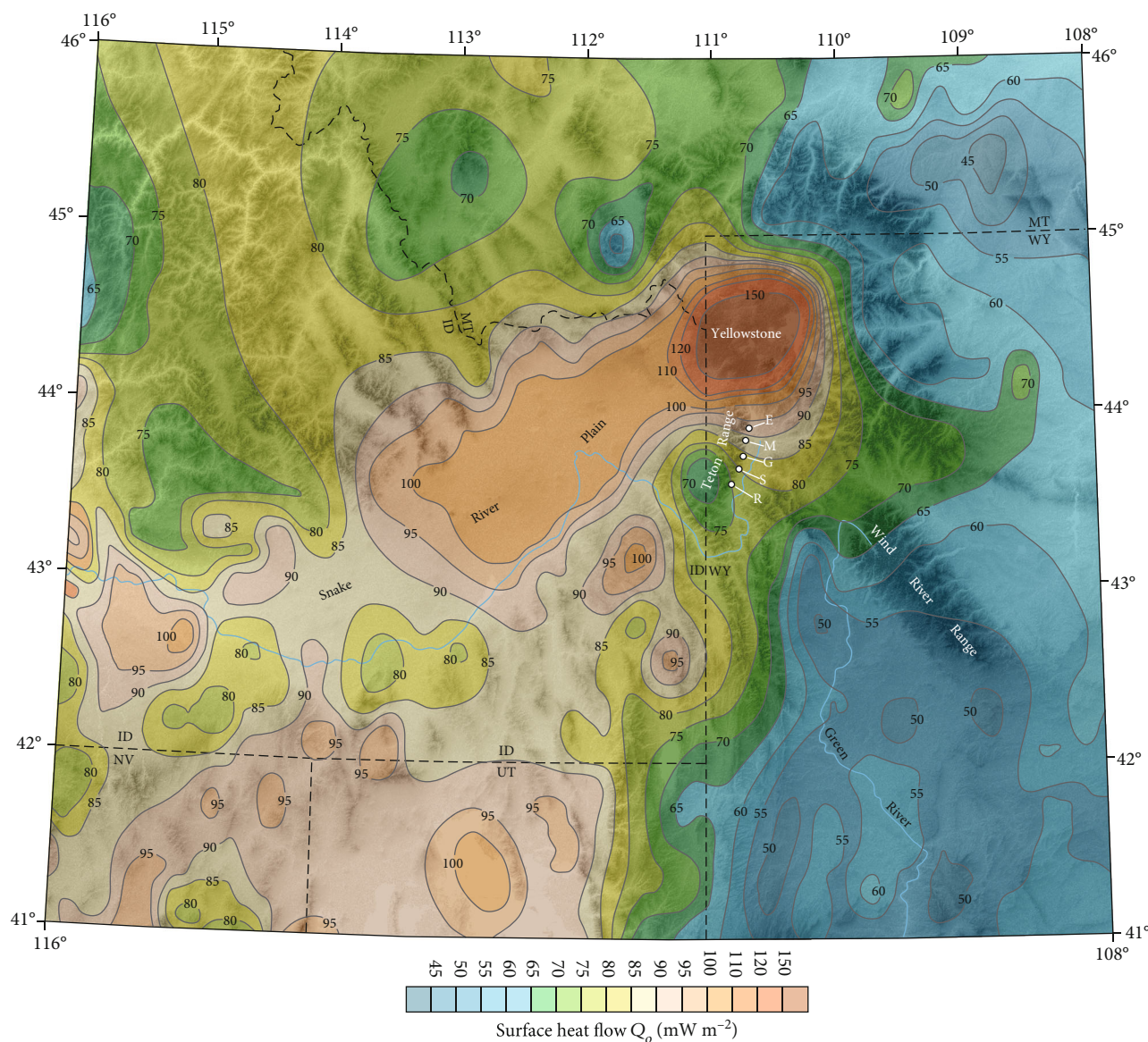
FIGURE 5: Surficial heat flow map of the Snake River plain, including the greater Teton-Yellowstone region. Modified from [42]. The highest heat surficial heat flows (~150 mW m^{-2}) in the region are recorded in the modern Yellowstone caldera, but these values decrease substantially to the south into the Teton Range. This north-south gradient in measured surficial heat flow is used as a key constraint for the geothermal gradient models of this study. R: Rendezvous; S: Static Peak; G: Grand Teton; M: Moran; E: Eagles Rest.

(Figure 10). Based on the flexural-kinematic modeling, footwall uplift (U_{fw}) can be related to total displacement (x) by a simple linear relationship:

$$U_{fw} = 0.2457x. \tag{4}$$

This equation is used to calculate total displacement (x) from estimated footwall uplift values determined from inverse thermal history and geothermal gradient modeling.

4. Discussion

4.1. Onset and Slip History for the Teton Fault. Two periods of relatively rapid cooling were identified in the inverse thermal history models, with the exception of the Eagles Rest

transect, which currently yields only one pronounced cooling event (Figures 3 and 4). In all transects, the more recent event is interpreted to represent the final phase of Teton fault footwall exhumation that initiated in response to fault slip from ~10-8 Ma to present. Given that our sample locations lie in the immediate footwall of the Teton normal fault, we argue that this assumption is valid. These recent cooling trends, which are recognized in all five transects, can mostly be distinguished from the earlier cooling event which is discussed below. If the more recent event represents final Teton fault motion, it yields a Teton fault slip onset of 15-8 Ma, with the majority of transects yielding onset ages of 10-8 Ma.

The older cooling events predicted by some of the inverse thermal history models (Figures 3 and 4) are more difficult to reconcile, particularly because the credible

TABLE 7: Parameters used for calculating thermal gradients for the southern (Models 1-4), central (Models 5-8), and northern (Models 9-12) Teton Range. All models included a surface temperature (T_o) of 4 °C, a thermal conductivity (K) of 3 W m^{-1} K^{-1}, and a crustal thickness (y_c) of 30 km.

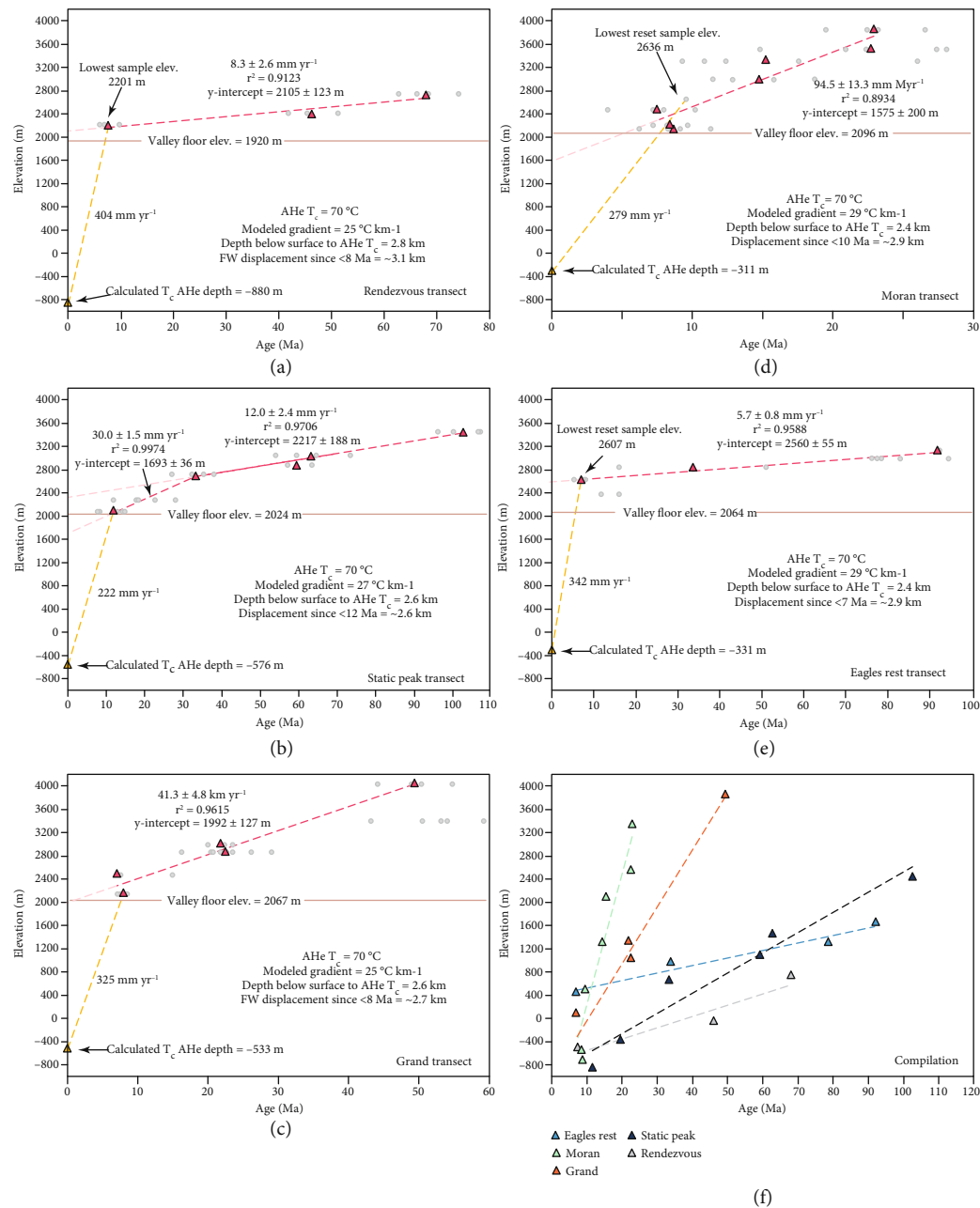|	Model 1	Model 2	Model 3	Model 4	Model 5	Model 6	Model 7	Model 8	Model 9	Model 10	Model 11	Model 12
Surface heat flow Q_o (W m^{-2})	0.075	0.075	0.075	0.075	0.081	0.081	0.081	0.081	0.087	0.087	0.087	0.087
Mantle heat flow Q_m (W m^{-2})	0.075	0.045	0.030	0.015	0.081	0.051	0.036	0.012	0.087	0.057	0.042	0.027
Radiogenic heat prod. A (W m^{-3})	0	$1.0E^{-6}$	$1.5E^{-6}$	$2.0E^{-6}$	0	$1.0E^{-6}$	$1.5E^{-6}$	$2.0E^{-6}$	0	$1.0E^{-6}$	$1.5E^{-6}$	$2.0E^{-6}$

FIGURE 6: AHe age-elevation relationships for (a) Rendezvous, (b) Static Peak, (c) Grand, (d) Moran, and (e) Eagles Rest transects. Gray circles are single grain ages, and red triangles are average ages for each sample. The red dashed line indicates a linear best-fit of age-elevation relationships for all samples along each transect. Two separate linear best-fit lines are calculated for the Static Peak transect to reflect the obvious inflection point in that data. Calculated depth to the AHe zero age (i.e., T_c depth) based on depth below the valley floor elevation of each transect and modeled geothermal gradients of 25˚C km^{-1} (Rendezvous), 27˚C km^{-1} (Static and Grand), and 29˚C km^{-1} (Moran and Eagles Rest) are shown as yellow lines on each plot. The total footwall uplift is calculated as the difference between the calculated T_c depth and the elevation of the lowermost sample for the Rendezvous, Static Peak, Grand, and Eagles Rest transects. For the Moran transect, total footwall uplift is calculated as the difference between the calculated T_c depth and the highest elevation sample that is interpreted to have been reset (i.e., below the depth of T_c) prior to the Miocene uplift of the Teton fault footwall. (f) Compilation age-elevation relationships for all transects. If the Teton fault behaved as a single tip-propagation normal fault, it would be expected that the transects that preserved the greatest displacement and thus represent the center of the fault would preserve the steepest age elevation gradients, with the gradient slope decreasing toward the fault tips. Mount Moran, which is here interpreted to represent the center of the Teton fault, records the steepest age-elevation gradient, and this gradient decreases progressively from the Grand, to Static Peak, and ultimately to Rendezvous Peak in the southern Teton Range. North of Mount Moran; however, the Eagle Rest Peak preserves an early gradient similar in slope to that recorded at Rendezvous Peak, but it also records the reset ages at much higher elevations than the three more southern transects, indicating a more complex motion history for the northern Teton fault.
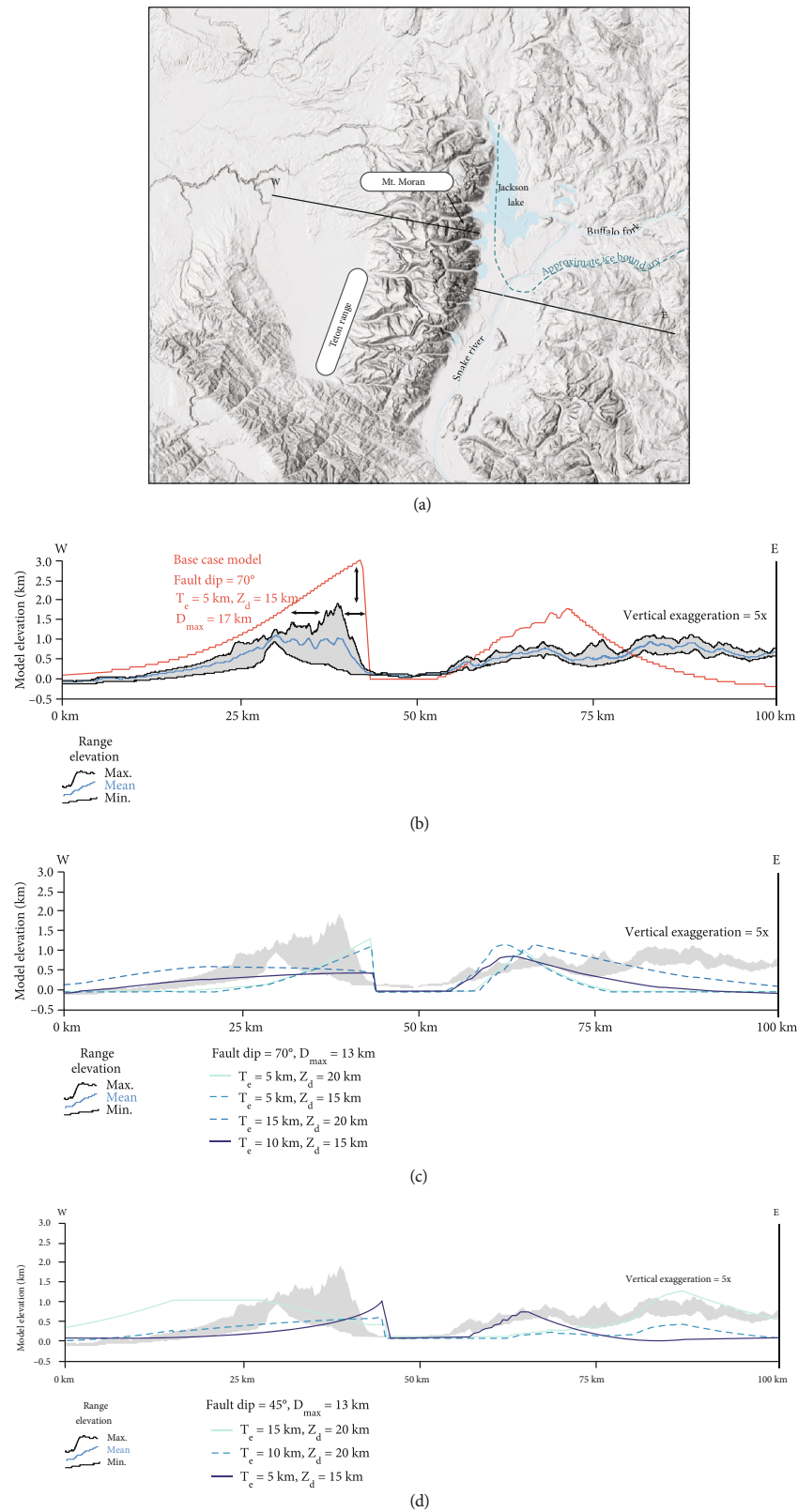
FIGURE 7: Modeled geothermal gradients produced for a range of parameters for basal mantle heat flow (Q_m, W·m^{-2}) and internal heat generation values (A, W·m^{-3}) to produce a range of surface heat flows (Q_o, W·m^{-2}) that can be compared with measurements of surface heat flow in the Teton-Yellowstone region. As can be seen in Figure 5, measured Q_o values of 0.075, 0.081, and 0.087 W m^{-2} are considered representative of the southern, central, and northern Teton AHe transects, respectively, yield geothermal gradient values of 26-29, 24-27, and 22-25°C km^{-1}. These values are similar to those measured by [41] in the southern and central Tetons. For Mount Moran, which is interpreted as the locus of maximum displacement (D_{max}) along the Teton fault, displacement is calculated using the highest geothermal gradient values of 26-29°C km^{-1}.

intervals increase substantially during the earlier cooling history. Also, because the inverse thermal history models include the implicit assumption that these transects are vertical, the ratio of the transect relief to the lateral distance of the transect from the fault plane will control how much of the history the transect records (greater relief records more of the cooling history) and the degree to which the AHe ages reflect fault motion (samples further from the projected fault plane will have a cooling history that is less influenced by fault slip-related cooling). In the Teton example, the most recent 15-8 Ma uplift event is predicted from the relatively young low-elevation AHe ages, but because the higher elevation samples along each transect were collected at substantially different distances from the fault plane, the response of the ages to fault motion (and the subsequent cooling and landscape response) could be impacted by such transect artifacts.

Because of these possible sampling-related artifacts, we chose to focus on the two transects (Static Peak and Moran) that include the highest total relief and are laterally closest to the interpreted Teton fault plane when interpreting this earlier cooling event (Figures 3(b) and 4(a)). Inverse thermal history models of the Static Peak and Moran transects both yield a pronounced Oligocene-Miocene cooling event (30-

20 Ma) that precedes the most recent 15-8 Ma cooling event. This cooling pattern, which we interpret to be related to slip on the Teton fault, can be clearly distinguished in along-strike plots of AHe ages that highlight the variable magnitude of cooling along strike (Figure 11). Because this earlier cooling event significantly postdates the most recent phase of Laramide orogenesis in the region (Laramide, Cretaceous-Paleocene) [48], we provisionally interpret this earlier cooling event to result from the earliest normal motion on the Teton fault. If correct, this would make the Teton fault one of the oldest Basin and Range structures [49]; however, we emphasize that this interpretation remains provisional until further data and analysis can be completed in a future study.

4.2. Footwall Exhumation from Inverse Thermal History Modeling. For the most recent cooling event predicted by the inverse thermal history models, which is interpreted to reflect Teton fault motion from 15-8 Ma to present, footwall cooling estimates can be integrated with the modeled geothermal gradients to calculate footwall exhumation magnitudes. For clarity, footwall cooling is the total cooling of the highest elevation footwall sample that yields a reset AHe age (i.e., an age younger than the age of fault slip onset) from each transect and footwall exhumation is calculated by

(a)

(b)

(c)

(d)

FIGURE 8: (a) Location of topographic swath profile used by [30] to compare with flexural-kinematic model results. Footwall swath is moved south of the Yellowstone ice cap boundary in order to capture the flexural bulge removed by the ice cap. (b) Base case model used for calculating the contributions of footwall uplift and hanging wall drop to total fault displacement. Difference between the modeled profile (orange) and the observed profile (blue and gray) results from a lack of footwall erosion in the modeled profile. (c, d) Additional model results of [30] and comparisons with the observed topography.
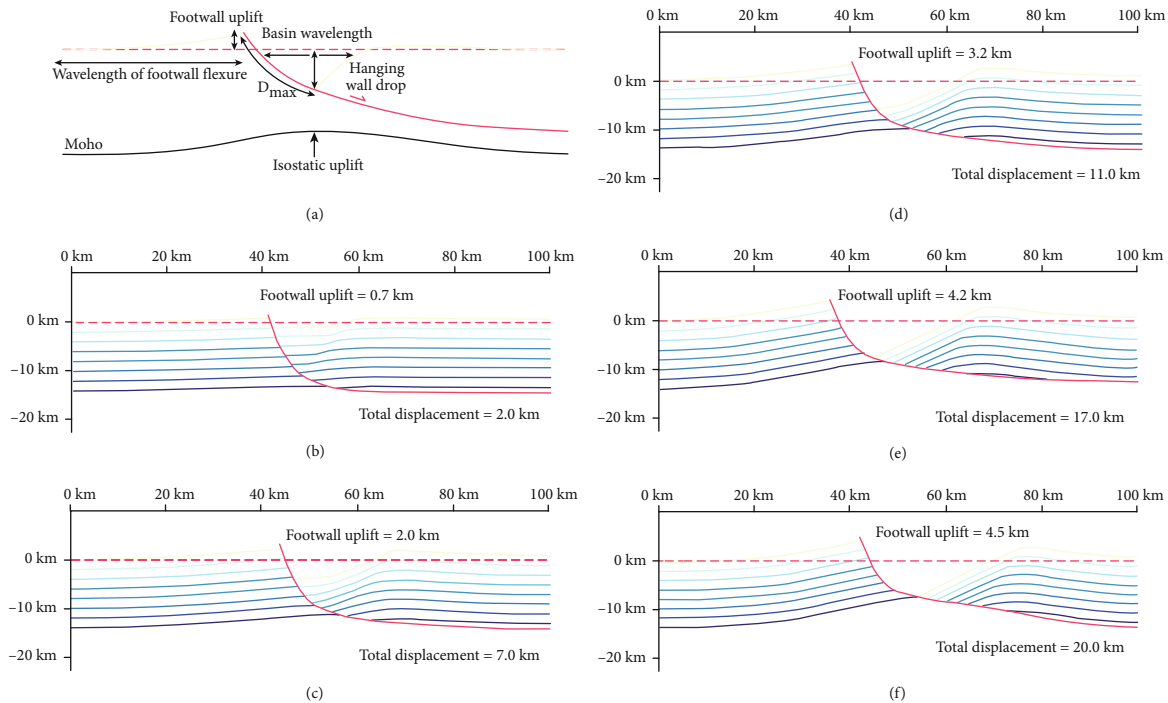
FIGURE 9: Result of the base case flexural-kinematic models of [30] that are used to establish the footwall uplift and hanging wall drop components of total displacement on the Teton normal fault system. (a) Model set-up, showing footwall uplift isostatic response to normal fault motion. The basin in this simple model is not filled with sediment. The basin wavelength and the wavelength of footwall flexure were used to compare with the topographic swath profile shown in Figure 8. Flexural-kinematic model results for total displacement values of (b) 2.0 km, (c) 7.0 km, (d) 11.0 km, (e) 17.0 km, and (f) 20.0 km.
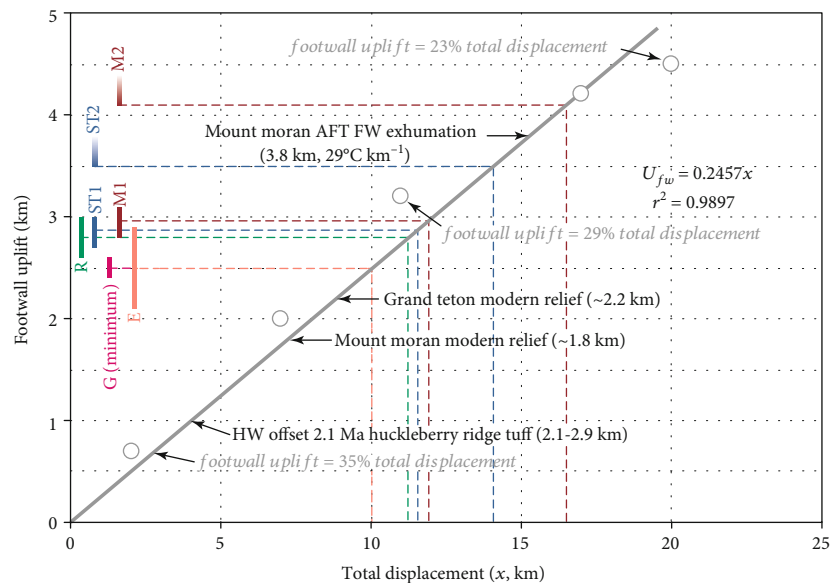
FIGURE 10: Footwall uplift vs. total displacement magnitude as derived from the flexural-kinematic models (white circles). Gray line represents the linear best-fit for the modeled response in Figure 9 (white circles with gray outlines). is a second-order polynomial. M1 (Moran), ST1 (Static Peak), R (Rendezvous), G (Grand Teton), and E (Eagles Rest) represent footwall uplift and associated total displacement values for the latest phase of cooling predicted by the inverse thermal history models. The G value is considered to be a minimum value. Importantly, all the footwall uplift estimates are greater than the maximum footwall relief observed in the vicinity of the Grand Teton. The M2 (Moran) and ST2 (Static Peak) values represent calculated footwall uplift and associated total displacement values if the total cooling of those transects includes the older Oligocene-Miocene cooling event.
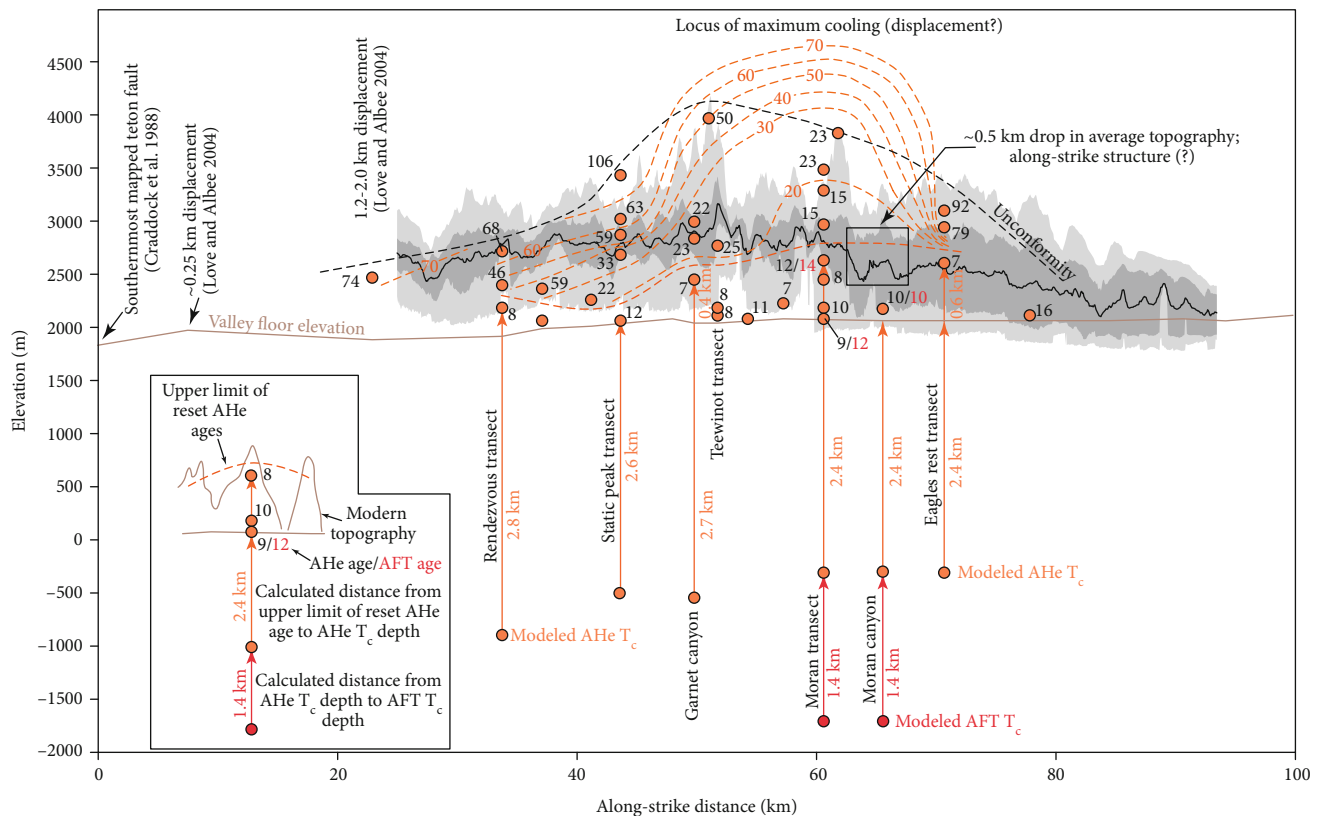
FIGURE 11: Schematic diagram of along-strike distribution of AHe and AFT data, fault trench locations, and the mapped position of the southern Teton fault tip underlain by along-strike swath topographic profiles of the present-day Teton Range. The highest elevation position of the base Paleozoic unconformity is offset to the south of the maximum exhumation magnitude of the Teton footwall near Mount Moran, as inferred from AHe isochrons (orange dashed lines). The clear ~0.5 km drop in mean topographic elevation as indicated in swath topographic profiling [63] occurs immediately north of Mount Moran and coincides with the downward shift in the oldest AHe ages at Eagles Rest compared to equivalent elevations on Mount Moran and the abrupt eastern shift of the modern Teton fault scarp. This break is provisionally interpreted as a down-to-the-north normal fault that forms normal to the Teton fault but roughly parallel to the Snake River plain, similar to numerous structures mapped by [66].

integrating the maximum modeled geothermal gradient for each transect with total cooling. These calculations yield base case footwall exhumation magnitudes of 2.6-3.0 km (25° C km^{-1}, 64-76°C) for Rendezvous Peak, 2.7-3.0 km (27° C km^{-1}; 73-81°C) for Static Peak, 2.4-2.6 km (27° C km^{-1}; 66-70°C) for Grand Teton, 2.8-3.1 km (29° C km^{-1}; 82-91°C) for Mount Moran, and 2.1-2.8 km (29° C km^{-1}; 61-81°C) for Eagles Rest Peak. These estimates only consider the total cooling that occurred during the most recent rapid cooling event commencing at 10-8 Ma (Figures 3 and 4). If the earlier Oligocene-Miocene cooling event predicted in the Moran and Static Peak models is considered a part of the total Teton fault slip history, then these two transects yield footwall exhumation estimates of 4.1 km (29° C km^{-1}; ~120°C) and 3.5 km (27° C km^{-1}; ~95°C), respectively. As the Moran transect yields the greatest footwall cooling and consequently the greatest calculated footwall exhumation of all the transects analyzed, the Moran region is here interpreted to represent the approximate center of the Teton fault, following [10]. Thus, maximum displacement (D_{max}) for the Teton fault is calculated below using the Moran footwall exhumation values.

The cooling magnitudes derived from the inverse thermal history models and the calculated footwall exhumation magnitudes can also be compared with similar estimates derived from AHe age-elevation relationships (Figure 6), which can be useful for simple determinations of fault slip rate variations and total exhumation magnitudes. In this relatively simple analysis, it is assumed that the closure T of the AHe system is ~70°C [50, 51], the geothermal gradient is the same as that used for the inverse thermal history model of each transect, and any sample with an AHe younger than the age of fault onset as predicted by the inverse thermal history was buried at a depth greater than the AHe T_c prior to the onset of the latest Teton fault motion (~15-8 Ma). Thus, the difference between the elevation of the highest sample with an AHe age younger than the age of fault slip onset and the predicted depth to the AHe T_c yields the predicted total exhumation for each transect. In the southern and central Teton Range, this exercise yields footwall exhumation magnitudes of ~3.1, ~2.6, and~2.7 km for the Rendezvous, Static Peak, and Grand transects, respectively. In the northern Teton Range, these calculations yield footwall exhumation estimates of ~2.9 km for both the Moran and
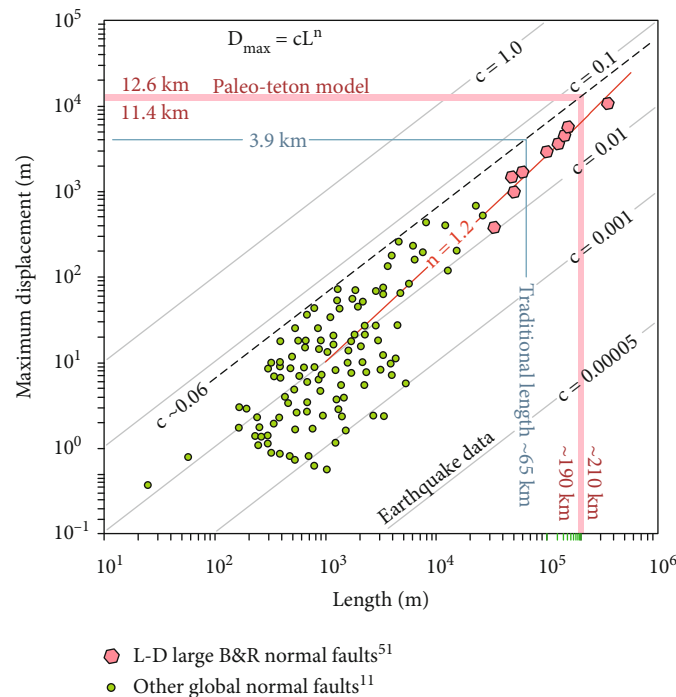
FIGURE 12: Fault length (L) maximum displacement (D_{max}) scaling relationships for normal faults with observed lengths of 10^1 m to 10^6 m modified from [11]. Most faults with $L > 104$ m yield D_{max} values equal to cL^n, where c ranges from 0.10 to 0.01 and n ranges from 1.0 to 1.2 (blue line) to 1.4 (red line). The global normal fault dataset (green circles) shows that faults are not observed to have displacement that is greater than ~6% ($c = 0.06$, black dashed line) of the length of the fault. Data derived from [67–72]. Other large basin and range normal faults (pink hexagons) [53] generally follow an $L – D$ relationship with $n = 1.2$ (red line). For estimated base case D_{max} values of 11.4-12.6 km determined from AHe and AFT data at Mount Moran, expected fault lengths should be 190-210 km, based on a relatively conservative scaling relationship with $c \sim 0.06$ that yields length estimates between n values of 1.2 to 1.4. If the presently preserved length (~65 km, light blue line) of the Teton fault represents the total length through time, it should only preserve ~3.9 km of total displacement, which is less than footwall uplift determined by this study.

Eagle Rest transects. If the Oligocene-Miocene cooling event is included for the Static Peak (31-23 Ma) and Moran (25-19 Ma) transects, a similar analysis yields total exhumation magnitudes of 3.3 and 4.1 km, respectively. All of these estimates are very similar to the footwall exhumation estimates calculated from the total cooling.

4.3. Total Displacement Analyses. The calculated footwall exhumation derived from the inverse thermal history models to determine the range of possible D_{max} values for the Teton fault. To do this requires the implicit assumption that the magnitude of footwall uplift due to fault displacement is approximately equal to the calculated magnitude of exhumation of the lower elevation samples along the transect that yield reset AHe ages. This assumption should generally hold true here, as the samples being exhumed in the lower part of the transect were hotter than the AHe T_c when the final phase of Teton fault slip begins. As discussed above, [30] evaluated how parameters such as surface fault dip, T_e, Z_d, and displacement will influence the varying contributions of footwall uplift and hanging wall drop contribute to D_{max}. Using the linear relationship between footwall uplift and total displacement derived from the base case flexural-kinematic model of [30] that provided the best match to

the modern day flexural profile (Figure 8; fault dip = 70°, $T_e = 5$ km, $Z_d = 15$ km) yields minimum calculated D_{max} values of 11.4-12.6 km for Mount Moran footwall uplift of 2.8-3.1 km for the most recent phase of footwall cooling. If the exhumation estimate included the Oligocene-Miocene cooling event identified in the inverse thermal history models, this would yield total displacement values of at least 16.7 km. Because that earlier event remains poorly constrained and will be the focus of a future study, we currently consider the displacement estimates of 11.4-12.6 km to represent a minimum D_{max} for the most recent phase of Teton fault motion. Displacement estimates for the other transects are included in Figure 10.

4.4. Length of the Paleo-Teton Fault. If the calculated displacement for the Moran transect represents D_{max} for the entire Teton fault, that value can be used to estimate the original length of the paleo-Teton fault. Studies of fault dimensions spanning more than eight orders of magnitude ([11] and references therein, [52]) demonstrate a near linear scaling between fault length (L) and displacement and show that D_{max} is always ~1 to 6% of L for large faults ($D_{max} > 104$ m; Figure 12). Using the conservative assumption that D_{max} is 6% of L in this case, displacement estimates
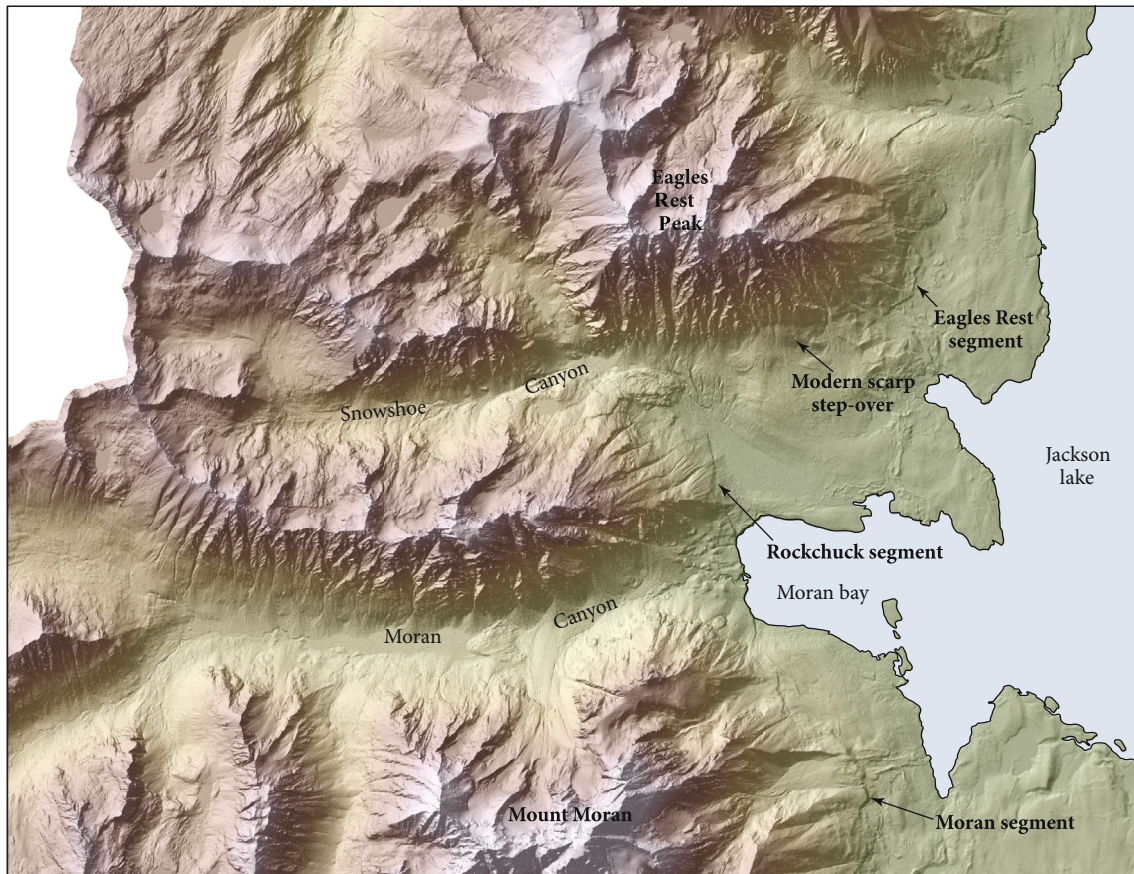
FIGURE 13: DEM (National Park Service, 2014) showing the linkage patterns of the modern Teton fault scarp segments between Mount Moran and Eagles Rest Peak (location shown on Figure 2). This zone coincides the position of a major stepover in the modern fault scarp at Snowshoe Canyon, a pronounced ~0.5 km drop in average topography, based on topographic swath profiling of [63], a pronounced increase in AHe ages at equivalent elevations between Mount Moran and Eagles Rest. This is provisionally interpreted to represent a down-to-the-north zone of motion normal to the main Teton fault, similar to normal fault zones mapped parallel to the Snake River plain by [64]. The precise position of the structures that accommodate this motion remains unclear but will be the focus of future detailed mapping efforts.

from the Mount Moran transect would yield a minimum estimated fault length of 190-210 km, which is consistent with length-displacement scaling relationships of other major Basin and Range normal faults (e.g., [53]), including the Wasatch fault [54, 55]. Provided that Mount Moran represents the approximate paleo-fault center, the Teton fault would have extended a minimum of ~85-105 km north and south of Moran prior to the onset of Huckleberry Ridge volcanism in the Yellowstone hotspot at ~2 Ma [56, 57]. These projections assume that fault propagation was not limited by interaction with other major structures. South of Mount Moran, the Teton fault continues for ~40 km prior to intersecting and offsetting the Laramide Cache Creek thrust [58]. South of that point, detailed mapping by multiple studies indicates that the Teton fault continues at least 30 km further south [59–61], yielding a minimum mappable southern extent at least 70 km south of Mount Moran.

To the north, the modern topographic expression of the Teton fault footwall only extends ~20 km and modern fault scarps that are possibly associated with modern Teton fault motion only extend another ~5 km [28], which is substan-

tially less than fault lengths predicted by $L - D_{max}$ relationships. As such, we interpret that the Teton fault and its associated footwall topography originally continued at least 85-105 km north of Mount Moran, 55-65 km farther than currently recognized. Because inverse thermal history models indicate that most of the Teton fault motion and related footwall topography development had accrued prior to multiple VEI 8 (volcanic explosivity index) supercaldera eruptions, including the Huckleberry Ridge (~2.0 Ma), Mesa Falls (~1.3 Ma), and Lava Creek (~0.6 Ma), we interpret that this northern paleo-Teton Range was removed/diminished following these events. In this scenario, if the Teton fault were to follow the same approximate trend, it would have extended at least as far north as Yellowstone Lake. At Mount Moran, the inverse thermal history models indicate that the lowest elevation sample had cooled to ~20°C by the onset of Huckleberry Ridge volcanism at ~2.0 Ma, and thus, all but <1.0 km of total footwall uplift was in place at that time.

4.5. Removal of the Paleo-Teton Mountain Range. Although limited direct evidence currently exists to determine what

happened to the northern extent of footwall topography, it is possible that some of the range was removed by collapse into the caldera either following the initial Huckleberry Ridge and later eruptive events or as a result of posteruptive isostatic collapse (e.g., [8]). Detailed mapping has shown that both the Huckleberry Ridge and Lava Creek [62] calderas would have transected the projected northern extension of footwall topography (Figure 2), but unfortunately, any structural or deformational evidence of the paleotopography removal north of this point would be buried by the subsequent rhyolite flows [28].

Flexural modeling was used to show that arching and subsidence of Paleozoic strata and Mesozoic fold hinges in the ranges north of the eastern Snake River Plain could be accommodated by isostatic adjustment to a relatively dense midcrustal sill [28]. Models from that study showed downward flexure of 2.8-4.2 km of the upper crustal strata was possible, depending on the depth of compensation. P-wave seismic inversion was used to interpret a lower-crustal basaltic body beneath the present-day Yellowstone hotspot [40] that may produce a similar isostatic response to that modeled in [8]. Traditionally, the arching of the north dipping base Paleozoic unconformity observed on many of the Teton peaks was interpreted to act as a key pinning horizon that tracked normal motion on the Teton fault. However, contouring of the compiled AHe data (Figure 11) shows that the highest magnitude of recent cooling does not correspond to the arched shape of this unconformity, and thus, it may be possible that the northern dip on the unconformity, like the Paleozoic units north of the Snake River plain, may be the result of such subsidence. Additionally, the contoured AHe data shows a pronounced and abrupt break in AHe ages between the Mount Moran and Eagles Rest transects, with much older AHe ages observed along the Eagles Rest transect at equivalent elevations to samples on the Moran transect. Provisionally, we interpret this to indicate that Eagles Rest Peak and the associated topography to the north may have experienced postfault motion subsidence (down-to-the-north) along a structure normal to the Teton fault. Coincidentally, this break, which is approximately located between Mount Moran and Eagles Rest Peak, also corresponds to (1) a pronounced eastern shift in the modern Teton fault scarp on the south side of Eagles Rest Peak at Snowshoe Canyon (Figure 13) and (2) an abrupt drop of the northern Teton average elevation by ~0.5 km between Mount Moran and Eagles Rest Peak, as indicated from along-strike topographic swath profiling (Figure 11) [63]. Although the nature, genesis, and kinematics of this topographic break will form part of a future study, it is possible that this structure may act in a similar fashion to the hotspot track parallel normal faults recognized along the Snake River plain [61].

5. Conclusions

New inverse thermal history models based on a compilation of new and previously existing AHe+AFT data is combined with new models of variable geothermal gradients along-strike of the Teton Range to define the timing of Teton fault slip and the total magnitude of exhumation, as a function of cooling. These results are combined with flexural-kinematic modeling to determine the total displacement magnitude accrued on the Teton fault at multiple transects, and to identify the maximum accumulated displacement ($D_{\max}$) that occurred in the vicinity of Mount Moran, which leads us to interpret that area as the approximate center of the paleo-Teton fault. These displacement estimates are then combined with fault length-displacement scaling relationships of global normal fault datasets to demonstrate that the Teton fault and its associated footwall topography comprising the Teton Range may have originally been much longer than the present-day topographic expression. In this scenario, we interpret that the northern paleo-Teton Range extended 85-105 km north of Mount Moran, well into the footprint of the modern Yellowstone hotspot track. Additionally, because our inverse thermal history models indicate that Teton fault slip onset started at least by 15-8 Ma (and possibly even earlier in the Oligocene), we interpret that most of the displacement had accumulated on the Teton fault prior to migration of the Yellowstone hotspot into its current position. In this scenario, the northernmost paleo-Teton Range would have been removed following the Huckleberry Ridge (~2.0 Ma) and later eruptions and/or subsided as a part of an isostatic response to a dense basalt body in the lower crust beneath Yellowstone, similar to the interpreted evolution of multiple mountain ranges along the northern edge of the Snake River plain. Some of this topographic reduction may have been accommodated by down-to-the-north structures provisionally indicated by multiple lines of evidence. This relatively rapid removal of mountain topography (<2 Myr) represents a potentially significant control on continental physiography, biogeography, continental-scale fluvial drainage, and climate over relatively short time spans.

References

[1] J. F. Dewey, "Extensional collapse of orogens," *Tectonics*, vol. 7, no. 6, pp. 1123–1139, 1988.

[2] P. England and G. Houseman, "Extension during continental convergence, with application to the Tibetan Plateau," *Journal of Geophysical Research: Solid Earth*, vol. 94, no. B12, p. 17561, 1989.

[3] P. Bird, "Lateral extrusion of lower crust from under high topography in the isostatic limit," *Journal of Geophysical Research*, vol. 96, no. B6, p. 10275, 1991.

[4] O. Vanderhaeghe and C. Teyssier, "Crustal-scale rheological transitions during late-orogenic collapse," *Tectonophysics*, vol. 335, no. 1-2, pp. 211–228, 2001.

[5] D. W. Burbank, "Rates of erosion and their implications for exhumation," *Mineralogical Magazine*, vol. 66, no. 1, pp. 25–52, 2002.

[6] B. Wernicke, "Low-angle normal faults in the Basin and Range Province: nappe tectonics in an extending orogen," *Nature*, vol. 291, no. 5817, pp. 645–648, 1981.

[7] E. T. Ruppel, *Geology of pre-Tertiary rocks in the northern part of Yellowstone National Park, Wyoming*, Geology of Yellowstone National Park: U.S. Geological Survey Professional Paper 729-A, 1972.

[8] N. McQuarrie and D. W. Rodgers, "Subsidence of a volcanic basin by flexure and lower crustal flow: The eastern Snake River Plain, Idaho," *Tectonics*, vol. 17, no. 2, pp. 203–220, 1998.

[9] R. L. Christiansen, *The quaternary and Pliocene Yellowstone plateau volcanic field of Wyoming, Idaho, and Montana*, USGS professional paper 729-G, 2001.

[10] S. J. Brown, J. R. Thigpen, J. A. Spotila, W. C. Krugh, L. M. Tranel, and D. A. Orme, "Onset timing and slip history of the Teton fault, Wyoming: a multidisciplinary Reevaluation," *Tectonics*, vol. 36, no. 11, pp. 2669–2692, 2017.

[11] M. A. E. Curry, J. B. Barnes, and J. P. Colgan, "Testing fault growth models with low-temperature thermochronology in the northwest Basin and Range, USA," *Tectonics*, vol. 35, no. 10, pp. 2467–2492, 2016.

[12] J. O. D. Byrd, R. B. Smith, and J. W. Geissman, "The Teton fault, Wyoming: topographic signature, neotectonics, and mechanisms of deformation," *Journal of Geophysical Research*, vol. 99, no. B10, pp. 20095–20122, 1994.

[13] P. M. Lavin and W. E. Bonini, "Detailed gravity measurements in the Teton Range and Jackson Hole, Wyoming," *GSA Bulletin*, vol. 68, p. 1760, 1957.

[14] J. S. Behrendt, B. L. Tibbetts, W. E. Bonini, and P. M. Lavin, "A geophysical study in Grand Teton National Park and vicinity, Teton County, Wyoming," *US Geological Survey Professional Paper*, vol. 516-E, p. 23, 1968.

[15] B. L. Tibbetts, J. C. Behrendt, and J. D. Love, "Seismic-refraction measurements in Jackson hole, Wyoming," *GSA Bulletin*, vol. 80, no. 6, pp. 1109–1122, 1969.

[16] J. D. Love, "Summary of Upper Cretaceous and Cenozoic stratigraphy, and of tectonic and glacial events in Jackson Hole, northwestern Wyoming," in *Guidebook for the 29th Wyoming Geological Association Annual Field Conference*, pp. 585–593, 1977.

[17] J. D. Love, "Teton mountain front, Wyoming," in *Geological Society of America Centennial Guide: GSA, Rocky Mountain Section*, pp. 173–178, 1987.

[18] R. L. Christiansen and J. D. Love, *The Pliocene Conant Creek Tuff in the northern part of the Teton Range and Jackson Hole, Wyoming*, U.S. Geological Survey bulletin 1435-C, 1978.

[19] J. D. Gilbert, D. Ostenaa, and C. Wood, *Seismotectonic Study of Jackson Lake Dam and Reservoir, Minidoka Project, Idaho-Wyoming*, U.S. Bureau of Reclamation Seismotectonic Report, 1983.

[20] M. D. Petersen, A. D. Frankel, S. C. Harmsen et al., "Documentation for the 2008 update of the United States National Seismic Hazard Maps," U.S. Geological Survey Open-File Report 2008-1128, 2008.

[21] R. B. Smith, "Seismicity and earthquake hazards of the Borah Peak-Hebgen Lake-Yellowstone-Teton region – implications for earthquakes in extensional and active volcanic regimes," Geological Society of America Abstracts with Programs, 1988.

[22] R. B. Smith, J. O. D. Byrd, R. L. Bruhn, D. D. Susong, and A. G. Sylvester, "An Evaluation of Earthquake Hazards of the Grand Teton National Park Emphasizing the Teton Fault," vol. 14, Article ID 28, University of Wyoming National Park Service Research Center Annual Report, 1990.

[23] B. J. P. White, R. B. Smith, S. Husen, J. M. Farrell, and I. Wong, "Seismicity and earthquake hazard analysis of the Teton-Yellowstone region, Wyoming," *Journal of Volcanology and Geothermal Research*, vol. 188, pp. 277–296, 2009.

[24] C. B. DuRoss, R. D. Gold, R. W. Briggs et al., "Preliminary paleoseismology of the Buffalo bowl trench site on the Teton fault," *Seismological Research Letters*, vol. 89, p. 836, 2018.

[25] C. B. DuRoss, M. S. Zellman, G. D. Thackray, R. W. Briggs, R. D. Gold, and S. A. Mahan, "Holocene Paleoseismology of the Steamboat Mountain site: Eevidence for full-length rupture of the Teton Fault, Wyoming," *Bulletin of the Seismological Society of America*, vol. 111, pp. 439–465, 2020.

[26] M. S. Zellman, C. B. DuRoss, G. D. Thackray et al., "A paleoseismic investigation of the northern Teton fault at the Steamboat Mountan trench site, Grand Teton National Park, Wyoming," *Seismological Research Letter*, vol. 89, p. 837, 2018.

[27] R. B. Smith, J. O. D. Byrd, and D. D. Susong, "The Teton Fault, Wyoming: seismotectonics, quaternary history, and earthquake hazards," *Geological Survey of Wyoming Memoir*, vol. 5, pp. 628–667, 1993.

[28] M. S. Zellman, C. B. DuRoss, and G. D. Thackray, *The Teton Fault*, Wyoming Geological Survey Open File Report, Teton County, Wyoming, 2019.

[29] M. G. Bonilla, R. K. Mark, and J. J. Leinkaemper, "Statistical relations among earthquake magnitude, surface rupture, and surface fault displacement," *Bulletin of the Seismological Society of America*, vol. 74, pp. 2379–2411, 1984.

[30] A. L. Helfrich, "Testing interpretations of the displacement magnitude of the Teton fault and uplift of the Teton range, Wyoming with integrated flexural-kinematic and thermal modeling [M.S. thesis]," University of Kentucky, 2020.

[31] R. M. Hoar, "Refining the onset timing and slip history along the northern part of the Teton fault," [M.S. thesis] University of Kentucky, 2019.

[32] M. L. Swallom, "Determining rates of landscape response to tectonic forcing across a range of temporal scales and erosional mechanisms: Teton range, WY [M.S. thesis]," University of Kentucky, 2019.

[33] K. Gallagher, "Transdimensional inverse thermal history modeling for quantitative thermochronology," *Journal of Geophysical Research*, vol. 117, no. B2, p. B02408, 2012.

[34] W. R. Guenthner, P. W. Reiners, and U. Chowdhury, "Isotope dilution analysis of Ca and Zr in apatite and zircon (U-Th)/He chronometry," *Geochemistry, Geophysics, and Geosystems*, vol. 17, no. 5, pp. 1623–1640, 2016.

[35] R. M. Flowers, K. A. Farley, and R. A. Ketcham, "A reporting protocol for thermochronologic modeling illustrated with data from the Grand Canyon," *Earth and Planetary Science Letters*, vol. 432, pp. 425–435, 2015.

[36] K. Gallagher, "Comment on 'A reporting protocol for thermochronologic modeling illustrated with data from the Grand Canyon' by Flowers, Farley and Ketcham," *Earth and Planetary Science Letters*, vol. 441, pp. 211-212, 2016.

[37] R. M. Flowers, R. A. Ketcham, D. L. Shuster, and K. A. Farley, "Apatite (U-Th)/He thermochronometry using a radiation damage accumulation and annealing model," *Geochimica et Cosmochimica Acta*, vol. 73, no. 8, pp. 2347–2365, 2009.

[38] R. A. Ketcham, R. A. Donelick, and W. D. Carlson, "Variability of apatite fission-track annealing kinetics: III. Extrapolation to geological time scales," *American Mineralogist*, vol. 84, no. 9, pp. 1235–1255, 1999.

[39] R. A. Ketcham, A. Carter, R. A. Donelick, J. Barbarand, and A. J. Hurford, "Improved modeling of fission-track annealing in apatite," *American Mineralogist*, vol. 92, no. 5-6, pp. 799–810, 2007.

[40] H.-H. Huang, F. C. Lin, B. Schmandt, J. Farrell, R. B. Smith, and V. C. Tsai, "The Yellowstone magmatic system from the mantle plume to the upper crust," *Science Reports*, vol. 348, no. 6236, pp. 773–776, 2015.

[41] H. P. Heasler, "Geothermal modeling of Jackson Hole, Teton County Wyoming," Tech. Rep. 198723, Technical Report for the Department of Energy, NTIS, 1987.

[42] D. D. Blackwell and M. C. Richards, "The 2004 geothermal map North America: Exeplanation of resources and applications," *Geothermal Resources Council Transactions*, vol. 28, pp. 317–320, 2004.

[43] J. V. Pérez-Peña, M. al-Awabdeh, J. M. Azañón, J. P. Galve, G. Booth-Rea, and D. Notti, "SwathProfiler and NProfiler: Two new ArcGIS Add-ins for the automatic extraction of swath and normalized river profiles," *Computers and Geosciences*, vol. 104, pp. 135–150, 2017.

[44] B. Wernicke and B. C. Burchfiel, "Modes of extensional tectonics," *Journal of Structural Geology*, vol. 4, no. 2, pp. 105–115, 1982.

[45] P. Gans and E. L. Miller, "Geologic and geophysical constraints on the geometry of crustal extension in the east Basin and Range Province," *Geological Society of America Abstracts and Programs*, vol. 16, p. 515, 1984.

[46] J. Jackson and D. McKenzie, "The geometrical evolution of normal fault systems," *Journal of Structural Geology*, vol. 5, no. 5, pp. 471–482, 1983.

[47] A. B. Watts, *Isostasy and Flexure of the Lithosphere*, Cambridge University Press, 2001.

[48] J. M. English and S. T. Johnston, "The Laramide orogeny: what were the driving forces?," *International Geology Review*, vol. 46, no. 9, pp. 833–838, 2004.

[49] J. P. Colgan, T. A. Dumitru, and E. L. Miller, "Diachroneity of Basin and Range extension and Yellowstone hotspot volca-

nism in northwestern Nevada," *Geology*, vol. 32, no. 2, pp. 121–124, 2004.

[50] K. V. Hodges, "Thermochronology in orogenic systems," *Treatise on Geochemistry*, vol. 3, pp. 263–292, 2014.

[51] A. K. Ault, C. Gautheron, and G. E. King, "Innovations in (U–Th)/He, fission track, and trapped charge thermochronometry with applications to earthquakes, weathering, surface-mantle connections, and the growth and decay of mountains," *Tectonics*, vol. 38, no. 11, pp. 3705–3739, 2019.

[52] A. Rotevatn, C. A. L. Jackson, A. B. M. Tvedt, R. E. Bell, and I. Blækkan, "How do normal faults grow?," *Journal of Structural Geology*, vol. 125, pp. 174–184, 2019.

[53] A. L. Densmore, N. H. Dawers, S. Gupta, R. Guidon, and T. Goldin, "Footwall topographic development during continental extension," *Journal of Geophysical Research*, vol. 109, no. F3, p. F03001, 2004.

[54] W. T. Parry and R. L. Bruhn, "Fluid inclusion evidence for minimum 11 km vertical offset on the Wasatch fault, Utah," *Geology*, vol. 15, no. 1, pp. 67–70, 1987.

[55] P. A. Armstrong, A. R. Taylor, and T. A. Ehlers, "Is the Wasatch fault footwall (Utah, United States) segmented over million-year time scales?," *Geology*, vol. 32, no. 5, pp. 385–388, 2004.

[56] C. A. Gansecki, G. A. Mahood, and M. O. McWilliams, "$^{40}Ar^{39}Ar$ geochronology of rhyolites erupted following collapse of the Yellowstone caldera, Yellowstone Plateau volcanic field: implications for crustal contamination," *Earth and Planetary Science Letters*, vol. 142, no. 1-2, pp. 91–107, 1996.

[57] C. A. Gansecki, G. A. Mahood, and M. McWilliams, "New ages for the climactic eruptions at Yellowstone: single-crystal $^{40}Ar/^{39}Ar$ dating identifies contamination," *Geology*, vol. 26, no. 4, pp. 343–346, 1998.

[58] J. D. Love, J. C. Reed Jr., and A. C. Christiansen, *Geologic Map of Grand Teton National Park, Teton County, Wyoming*, U.S. Geological Survey Miscellaneous Investigations Series, I-2031, scale 1: 62,500, 1992.

[59] H. F. Albee, *Geologic Map of the Munger Mountain Quadrangle, Wyoming*, United States Geological Survey Map GQ-705, scale 1: 24,000, 1968.

[60] J. P. Craddock, A. A. Kopania, and D. V. Wiltschko, "Interaction between the northern Idaho-Wyoming thrust belt and bounding basement blocks, central western Wyoming," in *Interaction of the Rocky Mountain Foreland and the Cordilleran Thrust Belt*, C. J. Schmidt and W. J. Perry, Eds., vol. 171, pp. 333–352, Geological Society of America Memoir, 1988.

[61] D. Love and H. F. Albee, *Geologic map of the Jackson Quadrangle, Teton County, Wyoming*, Wyoming State Geological Survey Map LMS-9, scale 1: 24,000, 2004.

[62] L. A. Morgan, W. C. P. Shanks, J. B. Lowenstern, J. M. Farrell, and J. E. Robinson, *Geologic field-trip guide to the volcanic and hydrothermal landscape of the Yellowstone Plateau*, U.S. Geological Survey Scientific Investigations Report 2017-5022-P, 2017.

[63] Y. Zhu, J. M. Dortch, M. A. Massey, W. C. Haneberg, and D. Curl, "An intelligent swath tool to characterize complex topographic features: theory and application in the Teton Range, Licking River, and Olympus Mons," *Geomorphology*, vol. 387, p. 107778, 2021.

[64] K. L. Pierce and L. A. Morgan, "The track of the Yellowstone hot spot: volcanism, faulting, and uplift," in *Regional Geology of Eastern Idaho and Western Wyoming*, P. K. Link, M. A.

Kuntz, and L. B. Platt, Eds., vol. 179, pp. 1–53, Geological Society of America Memoir, 1992.

[65] K. L. Pierce and L. A. Morgan, "Is the track of the Yellowstone hotspot driven by a deep mantle plume? – Review of volcanism, faulting, and uplift in light of new data," *Journal of Volcanology and Geothermal Research*, vol. 188, no. 1-3, pp. 1–25, 2009.

[66] N. C. Zentner, "Neogene normal faults related to the structural origin of the eastern Snake River Plain, Idaho [M.S. thesis]," Idaho State University, Pocatello, ID, 1989.

[67] J. A. Opheim and A. Gudmundsson, "Formation and geometry of fractures, and related volcanism, of the Krafla fissure swarm, northeast Iceland," *Geological Society of America Bulletin*, vol. 101, no. 12, pp. 1608–1622, 1989.

[68] R. W. Krantz, "Multiple fault sets and three-dimensional strain: theory and application," *Journal of Structural Geology*, vol. 10, no. 3, pp. 225–237, 1988.

[69] J. J. Walsh and J. Watterson, "Distributions of cumulative displacement and seismic slip on a single normal fault surface," *Journal of Structural Geology*, vol. 9, no. 8, pp. 1039–1046, 1987.

[70] J. J. Walsh, A. Nicol, and C. Childs, "An alternative model for the growth of faults," *Journal of Structural Geology*, vol. 24, no. 11, pp. 1669–1675, 2002.

[71] N. H. Dawers and M. H. Anders, "Displacement-length scaling and fault linkage," *Journal of Structural Geology*, vol. 17, no. 5, pp. 607–614, 1995.

[72] C. H. Scholz and P. A. Cowie, "Determination of total strain from faulting using slip measurements," *Nature*, vol. 346, no. 6287, pp. 837–839, 1990.